Los Alamos
NATIONAL LABORATORY
EST. 1943

LA-UR-20-27448
Approved for public release; distribution is unlimited.

Title: Analytic Modeling of a Deep Shielding Problem

Author(s): Remedes, Tyler Joseph

Intended for: Dissertation Review

Issued: 2020-09-22

Disclaimer:
Los Alamos National Laboratory, an affirmative action/equal opportunity employer, is operated by Triad National Security, LLC for the National Nuclear Security Administration of U.S. Department of Energy under contract 89233218CNA000001. By approving this article, the publisher recognizes that the U.S. Government retains nonexclusive, royalty-free license to publish or reproduce the published form of this contribution, or to allow others to do so, for U.S. Government purposes. Los Alamos National Laboratory requests that the publisher identify this article as work performed under the auspices of the U.S. Department of Energy. Los Alamos National Laboratory strongly supports academic freedom and a researcher's right to publish; as an institution, however, the Laboratory does not endorse the viewpoint of a publication or guarantee its technical correctness.

ANALYTIC MODELING OF A DEEP SHIELDING PROBLEM

By

TYLER J. REMEDES

A DISSERTATION PRESENTED TO THE GRADUATE SCHOOL
OF THE UNIVERSITY OF FLORIDA IN PARTIAL FULFILLMENT
OF THE REQUIREMENTS FOR THE DEGREE OF
DOCTOR OF PHILOSOPHY

UNIVERSITY OF FLORIDA

2020

Abstract of Dissertation Presented to the Graduate School
of the University of Florida in Partial Fulfillment of the
Requirements for the Degree of Doctor of Philosophy

ANALYTIC MODELING OF A DEEP SHIELDING PROBLEM

By

Tyler J. Remedes

Dec 2020

Chair: James Baciak
Major: Nuclear Science and Engineering Program - Department of Material Science

Previous generations of scientists would make tremendous efforts to simplify non-tractable problems and generate simpler models that preserved the fundamental physics. This process involved applying assumptions and simplifications to reduce the complexity of the problem until it reached a solvable form. Each assumption and simplification was chosen and applied with the intent to preserve the essential physics of the problem, since, if the core physics of the problem were eliminated, the simplified model served no purpose. Moreover, if done correctly, solutions to the reduced model would serve as useful approximations to the original problem. In a sense, solving the simple models laid the ground-work for and provided insight into the more complex problem. Today, however, the affordability of high performance computing has essentially replaced the process for analyzing complex problems. Rather than "building up" a problem by understanding smaller, simpler models, a user generally relies on powerful computational tools to directly arrive at solutions to complex problems. As computational resources grow, users continue trying to simulate new, more complex, or more detailed problems, resulting in continual stress on both the code and computational resources. When these resources are limited, the user will have to make concessions by simplifying the problem while trying to preserve important details. In the context of MCNP, simplifications typically come as reductions in geometry, or by using variance reduction techniques. Both approaches can influence the physics of the problem, leading to potentially inaccurate

or non-physical results. Errors can also be introduced as a result of faulty input into a computational tool: something as simple as transposing numbers in a tally input can result in incorrect answers.

In this paradigm, reduced complexity computational and analytical models still have an important purpose. The explicit form of an analytic solution is arguably the best way to understand the qualitative properties of simple models [1]. In contrast to "building up" a complex problem through understanding simpler problems, results from detailed computational scenarios can be better explained by "building down" the complex model through simple models rooted in the fundamental or essential phenomenology. Simplified analytic and computational models can be used to 1) increase a user's confidence in the computational solution of a complex model, 2) confirm there are no user input errors, and 3) ensure essential assumptions of the simulation tool are preserved.

This process of using analytic models to develop a more valuable analysis of simulation results is named the results analysis methodology. The utility of the results assessment methodology and a complimentary sensitivity analysis is exemplified through the analysis of the neutron flux in a dry used fuel storage cask. This application was chosen due to current scientific interest in used nuclear fuel storage.

CHAPTER 1
INTRODUCTION AND MOTIVATION

1.1 Motivation

America is the largest producer of nuclear power in the world, with 98 reactors producing approximately 805 billion killowatt-hours of power in 2017 [2]. Despite being the largest producer of nuclear energy, the United states has not established a permanent used nuclear fuel storage facility. Instead, nuclear power plants store used fuel on site, many using storage casks or canisters. A Savanah River National Laboratory report states nearly 100,000 fuel assemblies are stored in more than 2,000 casks at 75 storage sites [3].

Fuel casks are designed to store and protect spent nuclear fuel while shielding power plant workers and others from harmful radiation generated by unstable radioisotopes created through the fission process. There does not exist a singular design of a spent fuel cask due to multiple companies designing fuel casks and various types of spent nuclear fuel which need to be stored. While each design is varied, there exist certain components which are found across many spent fuel cask designs. Spent fuel casks typically have a right cylindrical shape with layers of high atomic number and low atomic number materials, such as steel alloys and concrete respectively. Layering materials with different atomic numbers provides radiation shielding for both gamma rays and neutrons, which are the two most penetrating types of radiation emitted by radioisotopes present in the fuel (e.q., O-17, Cm-242, and Sr-90). High atomic number materials are used to mainly shield gamma rays, whereas low atomic number materials are used to mainly shield neutrons. For this reason, most spent fuel casks have an inner region where spent fuel is stored, an outer region made of low atomic number materials (i.e. concrete) and high atomic number materials (i.e. steel alloys). Layered materials are also utilized in baseplates and lids.

Materials in a spent fuel cask are specifically chosen to be multi-functional. Spent fuel casks must conduct heat away from spent fuel rods, protect fuel from damage, prevent proliferation of radioactive materials, as well as shield radiation. Heat conduction is

achieved by using materials with high thermal conductivities to draw heat away from spent fuel rods to the environment. Thick layers of materials, such as steel and concrete, protect the cask contents from environmental or other sources of damage (i.e. a hurricane or a cask being dropped during transportation). Casks are also designed to prevent proliferation by, for example, featuring welded lids or the addition of security tags to discourage unauthorized access to spent fuel. Finally, spent fuel casks are designed to shield employees and the public from the harmful radiation produced by decaying radioisotopes created in the fuel during the power making process.

If a cask inadequately performs any of the above functions, it may become necessary to open the cask for a visual inspection. This is a costly and time consuming endeavor. Greulich et. al. state the cost to re-open a cask could be in the millions of dollars and require man-months of time [4]. The process of opening a cask to visually inspect the contents also carries an increased risk of exposing workers to radiation. The high costs associated with opening a cask would certainly make visual inspection an unappealing option. Simulation based and experimental research has been motivated by the desire to develop a non-destructive assay technique to verify cask contents.

Analyzing the capabilities of technology to ensure the contents of a spent fuel cask has motivated many scientific investigations, with a large reliance on computational simulations [4–6]. Simulation results can then be correlated to experimental observations in order to identify promising techniques to inspect the interior of a cask without opening the cask. Neutron flux and dose are common measurable quantities sought after in the simulation and experimental works surrounding radiation shielding investigations of spent fuel casks. In reality, these two quantities are the same with the latter being a scalar multiple of the former. These works tend to be concerned with the neutron flux at or beyond the surface of the cask, since the radiation environment exterior to the spent fuel cask is potentially harmful to worker safety. Understanding the interior neutron flux is useful in any simulation studying the exterior neutron flux. The neutron flux at the

surface of the spent fuel cask is directly dependent on the physics occurring interior to the spent fuel cask. Ultimately, the behavior of the interior neutron flux is controlled by the configuration and choice of materials inside the fuel cask. The relationship between interior structure and exterior neutron flux has prompted many simulation investigations using radiation transport codes. Further, simulation tools are not only used to design non-destructive assay techniques, but are also used to validate radiation transport codes as applied to spent fuel casks.

Ideally, simulation results should be compared to a series of identical or similar experiments *and* numerous results from other computational and numerical tools, and analogous analytical models. Computational, numerical and analytical tools act complimentary to experiments, in that the former tend not to be limited by physical restraints such as, but not limited to, detector placement, experimental design challenges, personnel safety, and costs. Nonetheless, experimental data is highly sought after since analytical models only provide exact solutions for the most simplistic non-physical problems and computational and numerical tools only approximate solutions, albeit these approximations can be quite accurate. Unfortunately, limited amounts of experimental data result in an increased reliance on computational and numerical tools. To further exacerbate the issue, it is of utmost importance that conclusions can be confidently drawn from simulation results. In the case of spent fuel casks, human lives and livelihood depend on the correctness of simulation results. The results assessment methodology provides a way to ensure the appropriateness and inerrancy of computational and numerical tools.

The results assessment methodology formulates analogs which are designed to share phenomenological physics with its more detailed counterpart. A discussion motivating the use of analogs is, therefore, useful. Fickett describes analogs as a qualitative representation of the original, constructed, not derived, in order to maximize simplicity while minimizing loss important properties [7]. Further, analogs have the following benefits 1) exact solutions are simpler to find and more likely to exist, 2) mathematical rigor in determining

analytical solutions is reduced, and 3) salient physics is more readily observable after the removal of extraneous features. The simplified computational and analytical models used in this work are developed as analogs. Before further description of the analytical models acting as analogs in this work, it is important to discuss the processes of validation, verification, uncertainty quantification and sensitivity analysis as applied to general computational tools and to simulations of used fuel casks.

1.2 Practices for Code Reliability, Confidence, and Predictive Capability

The behavior of physical systems is commonly described using complex mathematical expressions, typically consisting of differential equations. Exact solutions of these equations (also variously known as analytical or closed-form solutions) tend to be limited to only the simplest scenarios. Indeed, the cost of exactly solving these equations often involves the extensive use of simplifying assumptions to reduce the complexity of an equation to a form where an analytical solution is possible. Approximating a differential equation as a series of coupled linear equations became an alternative to finding direct analytical solutions. Unfortunately, discretization introduces a degree of error into the solution proportional to the fidelity to which a problem was discretized. Further, discretization requires a high degree of computational rigor and, therefore, was not a realistic technique for solving differential equations until adequate advancements in computation had occurred. However, the modern-day advancement of computational power has motivated the development of tools which approximate the solutions of complex differential equations in broad sets of circumstances via approximation techniques, as opposed to simplifying assumption techniques that may yield closed-form solutions only in special cases.

These simulation tools, or simulation codes, often rely on algebraic calculations to approximate solutions of the complex differential equations which describe real-world physics. The processes of verification and validation generate evidence "that computer [codes] have adequate accuracy and level of detail for their intended use" [8]. Verification

assesses "the numerical accuracy of the solution to a computational model," and validation "addresses the physical modeling accuracy of a computational simulation by comparing the computational results with experimental data" [9]. Stated another way, verification studies if a code solves equations correctly, and validation investigates the utility of a code through comparison with experimental data. Beyond verification and validation, uncertainty quantification has been added to quantify the accuracy with which simulation codes predict outcomes. Sensitivity analysis can be considered a type of uncertainty quantification which stratifies input parameters based on degree of impact to the error of simulation results. A short description of verification, validation, and sensitivity analysis will now be discussed.

Verifying a simulation tool requires demonstrating that the code is approximately solving the underlying equations as intended by the code developer [10]. Two examples of verification methods are benchmarking and comparison to analytical models. In benchmarking, results from a simulation tool are compared to known solutions from experiments, numerical tools, or other verified simulation tools.

Validation is ensuring a simulation tool approximately solves a representative set of equations consistent with the applications of the code. Validation relies on comparing experimental, analytical or numerical results against simulation results and validation is conducted on an application specific situations. Simulation tools are validated for different applications on a case-by-case basis. Validation commonly requires experimental data for a given application. However, sometimes experimental data is limited or non-existent since experiments can be financially burdensome, potentially risky to public and worker health, or difficult to conduct due to proprietary reasons. Difficulties in obtaining experimental data have led to alternative methods for validation, namely comparison between simulation codes. This methods attempts to validate a code by comparing results with a previously validated simulation code for an application.

Verification and validation determine the accuracy of a simulation tool for a specific application, however, neither certifies the usage of a particular code in solving a problem. Rather, it is the responsibility of the analyst to ensure that a particular simulation is relevant to the solution of a problem - ensuring the simulation is made in accordance with the manner which the code is verified and validated. Uncertainty analysis and sensitivity analysis aid in this process.

Simulation tools require parameters, or data provided by the user, such as physical properties measured through experiments (e.q., cross section data, viscosity, or thermal conductivity. These values have associated error; measurement error is an example. Uncertainty quantification is concerned with quantifying the error on the final result due to the error of input parameters, as well as, error introduced by the simulation tool itself. Further, uncertainty quantification is not concerned with the truth of a model, rather how parameters effect the solution [11]. Sensitivity analysis improves on uncertainty quantification by identifying which parameters most influence the result.

The typical approach to computational sensitivity analysis requires performing many simulations where a change is made in each computation - an approach called the direct method [12]. This process requires excessive computational resources. Applying sensitivity analysis techniques to analytical models allows for the identification of sensitivities without requiring as much computational resources, a strength of analytical sensitivity analysis. Further, if an equation yields an analytical solution, the sensitivities of an equation to its parameters can be found with minimal computational resources and requires solving sensitivity equations only once.

The history of sensitivity analysis as applied to differential equations is broad and extensive, therefore, only previous research that pertains to this work will be discussed. The first methodology for sensitivity analysis was developed on linear electrical circuits by Bode in 1945 [13]. At that time, sensitivity analysis motivated the use of feedback in circuit design. From its origins in circuit control, sensitivity analysis permeated

many others fields of science, including nuclear engineering, and many methods were developed. McKay provides an introduction into basic definitions and concepts related to sensitivity analysis [14]. Cacuci unified and generalized the direct method and the perturbation methods of sensitivity analysis in 1980 based on Frechet-derivatives [12]. A year later, Cacuci further generalized his methodology to analyze systems of response along arbitrary directions using the Gâteaux-derivative (G-derivative). This non-linear operator determines system responses to multiple perturbations in input parameters simultaneously. In doing so, Cacuci developed the Forward Sensitivity Analysis Procedure (FSAP) and Adjoint Sensitivity Analysis Procedure. The FSAP will be used to find sensitivities of the linear differential equations in this work.

The overall purpose of performing verification, validation, uncertainty quantification, and sensitivity analysis procedures is to identify the accuracy of a particular code for given scenarios. Ultimately, a code user must decide if a code adequately simulates the problem and if the user can have confidence that the simulated results are an accurate portrayal of the real-world problem. While the processes of verification, validation, and uncertainty quantification have been and continue to be extensively developed, there exists a limitation - how can a code be validated if there is no experimental data for comparison? The purpose of this document is to introduce a methodology aimed at answering this question.

1.3 State of Current Used Fuel Cask Research

Interest in experimental and simulation work stems from the need to ensure the safety and security of spent fuel casks; since there is currently no long term, national storage plan. Before discussing how simulations have been used to study spent fuel casks, it is important to take an aside and discuss the verification and validation of a commonly used radiation transport simulation code, the Monte Carlo N-Particle (MCNP) simulation code.

MCNP has been extensively verified and includes a series of benchmark problems. Further, Mosteller compiled a list of documents which discuss verification efforts on

MCNP [15]. analytical models have also been used in validation efforts [16, 17]. analytical models provide an exact solutions against which simulation tools can be compared. However, exact analytical solutions are often only available for heavily simplified problems which do not represent physical systems. Nonetheless, excellent agreement has been achieved between simple MCNP models and analytical solutions. Verification is considered an activity in mathematics where a successful test demonstrates that the governing equations of a simulation tool were solved correctly [18]. Validation of a simulation code is undertaken after verification.

MCNP has also undergone general validation in multiple disciplines within nuclear engineering; including but not limited to radiation shielding [19], criticality [20], and intermediate and high-energy physics [21] where MCNP results were compared to simple experiments. In order to validate computational tools as applied to spent fuel casks, scientist have turned to a comparative method where results from other radiation transport codes are compared with MCNP [22, 23]. However, discrepancies between results from different simulation tools are attributed to different physics being included in each tool. While this may be the driving factor leading to the apparent disagreement, this conclusion would benefit from identifying the physics seen in one simulation tool and neglected in the other. Comparison with experiments and other simulation tools is a valid, imperative, and important technique for validating simulation results, but more analysis should be done in order to increase confidence that simulation results can be trusted.

There exists a limited body of experimental work which measured the radiation dose at or near the surface of various used fuel casks. Unfortunately, none of the experiments were conducted on HI-STORM 100 spent fuel casks. Hence, discussion of past experiments will include radiation measurements performed on any spent fuel cask, including but not limited to experiments compared to any radiation transport code. Thiele et. al. even include a comparison between experimental results and the results from two radiation transport simulation tools (comparing Monaco/MARVIC with SAS4/MORSE) [24].

Both simulation tools are developed as part of the Standardized Computer Analysis for Licensing Evaluation (SCALE) packages by Oak Ridge National Laboratory. Since these radiation transport codes are not used in this work, no further explanation of the codes will be given. The author's report concludes that simulation tools can be applied for the assessment of dry storage casks. While experimental validation of simulation results is arguably the best way to corroborate simulation results, it is still important to not treat experimental data as sacrosanct [18]. Experiments still include measurement and procedural errors, and without the validation of multiple experiments of the same cask, the result of a lone experiment should not be considered to validate or invalidate simulation results. There also exists a large number of various dry fuel storage casks and experimental data may not exist to validate simulation results against. Computational and numerical tools have proven useful as an alternative to experimental data. Ziock et. al. measure the thermal neutron and gamma ray radiation signatures from six different spent fuel cask designs; the HI-STORM 100 was not one of the six. The authors posit the radiation signature can be used as an identifier for for individual casks. Their experiments proved inconclusive resulting from limitations of the imaging devices used. Wharton et. al. used MCNP to determine the fraction of gamma rays which would be detected by a high purity germanium detector placed at the top surface of two spent fuel cask designs [25]. These simulations were used to determine the feasibility of a system designed to used passive gamma radiation to determine if a fuel bundle was present or absent from a spent fuel cask. The authors concluded that the thick shielding of the spent fuel casks measured sufficiently scattered radiation and the system was not capable of resolving discrete gamma ray peaks. This resulted in the measurements being stopped without fully testing the capabilities of the system. It should be noted, the MCNP results suggested the system was capable of performing the measurements and distinguishing between empty and filled fuel storage positions. This work serves as an example for the importance of corroborating simulation results with further investigations.

Simulation studies of the HI-STORM 100 spent fuel cask using MCNP are more numerous than experimental studies. Priest conducted an in-depth investigation of neutron and gamma flux and dose rates interior to a HI-STORM 100 spent fuel cask with the purpose of identifying an imaging system capable of withstanding the harsh environment inside the multi-purpose canister (MPC) [26]. The author performed simulations using multiple MPC configurations with used nuclear fuel from both pressurized water and boiling water reactors.

Harkness et. al. used MCNP to investigate the validity using helium-4 fast neutron detectors to determine if fuel had been removed from a HI-STORM 100 spent fuel cask [6]. This work describes a methodology to generate a source definition for MCNP based on data provided in the Next Generation Safeguards Initiative. This fuel rod composition data was aged using ORIGEN-S, a material irradiation and decay calculation code, to create an MCNP compatible source definition. A further description of this process will be provided later in this work. The neutron flux and energy spectrum at the surface of the cask were tallied as part of this investigation. From the results of MCNP simulations, the authors concluded that neutron spectroscopy was feasible using helium-4 detectors, however, confidently determining if all fuel was present in a sealed spent fuel cask required further investigation.

Miller et. al. determined the feasibility of using a mono-energetic photon source to verify the contents of a sealed HI-STORM 100 spent fuel cask [27]. The authors simulated photon transport through the spent fuel cask and found a 1000-fold reduction in the transmitted flux when a fuel assembly is present as compared to a reduction of two in the transmitted flux when there is no assembly present. The authors further corroborated their work using analytical calculations to predict the scale of the uncollided flux for when a fuel assembly is present and when there is no fuel assembly. The results from their analytical modeling agreed with corresponding MCNP simulations.

Kelly et. al. performed an uncertainty analysis in radiation dose exterior to a HI-STORM 100S (a variant of the HI-STORM 100 cask) spent fuel cask based on variabilities in concrete composition and density [28]. The authors state that density variations in the concrete have the largest effect on radiation shielding capabilities. Varying concrete composition mostly affected neutron and associated capture gamma ray dose rates.

Because of the interest in modeling radiation transport in spent fuel casks, research has not been limited to using MCNP as a simulation tool nor has it been limited to a single cask design. Gao et. al. use the radiation transport code MAVRIC (a radiation transport code developed by Oakridge National Laboratory and distributed in with the SCALE code package) to simulate neutron and gamma transport through a TN-32 spent fuel cask [29]. In this work, the authors explore the effect of two geometries and two sets of cross section data on the neutron and gamma fluxes at the surface of the cask. The authors used a detailed model which included details of individual fuel rods and a homogenous model which calculated a homogenous fuel definition that simplified the geometry in each fuel cell. The authors also used two sets of cross section data. The first set were continuous energy cross section data and the second were multigroup cross sections. The authors concluded that changes to the geometry of the problem had a larger effect on the result that changing how the cross section data was handled.

Interest in verifying cask contents has led to simulations investigating methods for tomographic imaging. These investigations rely on simulation tools as a proof of concept and to aid experimental design. Liao and Yang have used cosmic-ray muon simulations to aid in experimental design choices for a spent fuel cask tomography system [30, 31]. The authors used Geant4 (another radiation transport code) and MCNP to simulate cosmic-ray muon transport through a spent fuel cask as well as through a test setup to guide experimental design. The authors then conducted experiments using the prototype

muon imaging systems. The authors concluded they were able to detect a quarter of a missing fuel bundle located anywhere in the cask.

Greulich et. al. also investigated the possibly of tomographic imaging techniques in verifying the contents of a spent fuel cask [4]. The authors simulated neutron transport through a TN-32 spent fuel cask using MCNP. Using a beam source of neutrons incident at the surface of the cask, the uncollided flux of neutrons leaving the cask provides information which can be used to reconstruct an image of the interior of the cask.

The previously described works were all interested in either radiation dose or radiation flux values at or exterior to the surface of the cask. Since dose is directly proportional to flux, and since the exterior neutron flux is a direct result of how interior cask structure affects the interior flux, the aim of this work is to investigate the interior neutron flux so as to have the most general relevance to existing work. The neutron flux was chosen over other types of radiation as the governing equation for neutrons is linear and provides a basis and proof-of-concept for the results assessment methodology.

The body of work focusing on simulations of spent fuel cask is quite large, which demonstrates scientific interest in simulating spent fuel casks. However, experimental data to validate simulated results is limited. Further, the final safety analysis report delivered by Holtec when licensing the HI-STROM 100 spent fuel canister system did not include any experimental data pertaining to the radiation shielding capabilities of this design [32]. Instead, MCNP was used to demonstrate the cask design was capable of attenuating radiation to an adequate level. Maintaining a safe environment for power plant workers and members of the public is of utmost importance and an alternate method for validating the accuracy of simulation results is needed if simulation results are to be relied upon in the absence of experimental data. The discrepancy between the amount of simulated results and experimental data identifies the need to validate or otherwise reinforce confidence in simulation results without relying on experimental data.

1.4 General Description of the Work

The results assessment and sensitivity analysis methods presented in this work act complimentary to existing techniques - verification, validation, uncertainty analysis, and sensitivity analysis- in order to develop a more valuable analysis. This work includes high-fidelity MNCP simulations of the interior neutron flux from a Holtec Hi-STORM 100 spent fuel cask, and the attendant analytical analysis of the simulation results in the absence of significant experimental validation data. A detailed model of the HI-STORM 100 spent fuel cask is simulated in MCNP to investigate the neutron flux interior to the fuel cask. Owing to a lack of validation data against which to compare these simulation results, an analytical analysis framework called "simulation results assessment" (or, henceforth, "results assessment") is developed and applied to provide an alternative (but not replacement) means for enhancing confidence in the computational model. The accuracy of the model is assessed by first developing simplified analytical and MCNP computational models. The design of these analogous models is made to retain essential physics while reducing geometric complexities. Since the essential physics is preserved, the neutron flux found using the analogous models will approximate the neutron flux interior to the cask of the detailed model. Developing analogous models is an iterative process where the initial simplified models were overly simplified and lost essential physics. Essential physics was identified from locations where disagreements between the results of the detailed model and the analogous models occur. More detailed analogs are developed in order to rectify differences observed between the two sets of results until a final set of analogous models are found. This process identified physical details that must be preserved in the detailed model in order for the detailed model to accurately simulate reality. A sensitivity analysis is also conducted on the final analogous model in each material region as well as on the detailed model in order to further validate the accuracy of the detailed model through the comparison of sensitivity structures between the models. This is also an iterative process which involves further refinement of analogous models

and input parameters in order to achieve comparable sensitivity structures between the detailed and analogous models. Finally confidence that the detailed model accurately simulates the interior neutron flux of a HI-STORM 100 spent fuel cask is increased after reaching comparable results and sensitivity structures between all models.

1.4.1 Results Assessment

A detailed model of this cask is developed in the MCNP code to predict the neutron flux in its interior. In an attempt to isolate essential physics, 1) five other MCNP simulations are developed to model various analogous problems, and 2) analytical models are developed to explain key characteristics of the flux seen in these analogous problems. The results of the simplified calculations are then used to reveal the fundamental physics controlling the shape and other characteristics of the flux distribution resulting from the complex model.This procedure is phenomenological in nature, and is thus intended to capture elemental physical processes that are occurring within sub-regions of the full-scale system. Therefore, while no single analytical solution is expected to be available for the full-scale system, any understanding gained in the sub-regions reinforces confidence that the integrated scales are being simulated in accordance with physical intuition. This outcome is valuable in cases where experimental data is sparse or nonexistent. A complimentary investigation of sensitivity structures produces a quantitative basis for comparison of analytical and computational models.

1.4.2 Sensitivity Analysis

The procedure of quantifying comparisons between analytical models, reduced geometry computational models, and the full model is demonstrated through the inclusion of sensitivity analysis procedures. Forward modeling of sensitivity structures is conceptually simple but computationally expensive for large problems, as it involves sampling a space of possible parameter values and executing a new simulation for each value. For analytical models the procedure is the opposite: using a generalized notion of the directional derivative, sensitivity structures can be computed in closed-form. The

comparison of these two methods forms the final component of this work. In addition to basic physics phenomenology, the sensitivity structure arising from analytical models can be compared to that found from forward sensitivity modeling of full-scale simulations. When these structures compare favorably, confidence in the full-scale simulations is once again reinforced.

1.5 General Overview of Chapters

This document discusses the rigorous analysis of a HI-STORM 100 used fuel cask using the results assessment methodology and a sensitivity analysis procedure. The results assessment methodology is discussed in chapters 2, 3, and 4, and chapters 5, 6 and 7 describe the process of adding a complimentary sensitivity analysis.

The second chapter of this document introduces the detailed MCNP model of the HI-STORM 100 used fuel cask. This model is used to demonstrate the results analysis methodology. The results of the simulated interior neutron flux are shown and features are identified in this chapter. A feature is defined in more depth in chapter 2.

Chapter 3 introduces the various analytical models used in this work. The neutron transport equation is derived and then reduced through application of assumptions and simplifications. From a reduced form of the neutron transport equation, the multigroup discrete ordinates equation and diffusion approximation are developed. The two equations form the basis of the analytical modeling used in this work.

The results assessment methodology is demonstrated in chapter 4. This chapter discusses why each analytical model is chosen as well as how each reduced complexity computational model is developed. After describing how the models are determined, each previously identified feature of the interior neutron flux is analyzed using the results assessment methodology.

Chapter 5 provides an overview into sensitivity analysis using the FSAP. A record of previous sensitivity analysis techniques is also provided. This chapter also introduces the sensitivity analysis process which will be used for the computational models in MCNP.

Chapter 6 provides foundational theory of the FSAP.

Comparisions between the FSAP analysis on analytical models and MCNP results are discussed in Chapter 7.

The last chapter includes final thoughts and conclusion regarding the work. Recommendations for future work are also provided in chapter 8.

CHAPTER 2
DISCUSSION OF MAIN PROBLEM

Dry storage casks provide protection, shielding, security, and cooling for used nuclear fuel which has spent at least one year in a spent fuel pool [33]. Shielding is especially important as used nuclear fuel is highly radioactive after being removed from a reactor and shielding is required to protect civilians, radiation plant workers, and the environment. The storage of used nuclear fuel has become a challenge in the United States since there is no long-term storage location. Instead, used nuclear fuel is stored in dry storage casks at the facility where it was generated. These casks are designed to 1) shield harmful radiation generated by the used nuclear fuel, 2) conduct decay heat away from fuel rods to prevent damage to the fuel and cladding, 3) protect spent nuclear fuel from environmental damage and other hazards, and 4) prevent proliferation of nuclear materials. Large efforts have been made in studying and designing casks to accomplish these challenges. While each function is imperative in analyzing the efficacy of a spent fuel cask, this work is only concerned with the radiation shielding capabilities of a Holtec International HI-STORM 100 spent fuel canister system.

Figure 2-1 is a diagram of the HI-STORM 100 spent fuel canister system partially loaded into an overpack of the same name. These two components together, the canister and overpack, will be referred to as a spent fuel cask. The HI-STORM 100 canister system is chosen as it is the most common used fuel storage system in the United States (750 canisters have been loaded before 2017) [3]. The overpack consists of two parts: a cylindrical dual material structure welded to a baseplate and a dual material removable lid. Both parts of the overpack use a combination of concrete and carbon steel to shield radiation, protect fuel, and prevent proliferation of nuclear material. Four vents are located at both the top and bottom of the overpack. These vents allow air to circulate between the overpack and MPC, removing heat caused by decaying isotopes in the spent fuel. Spent fuel rods are stored in the MPC, the central cylinder in Fig. 2-1. Figure 2-2 is

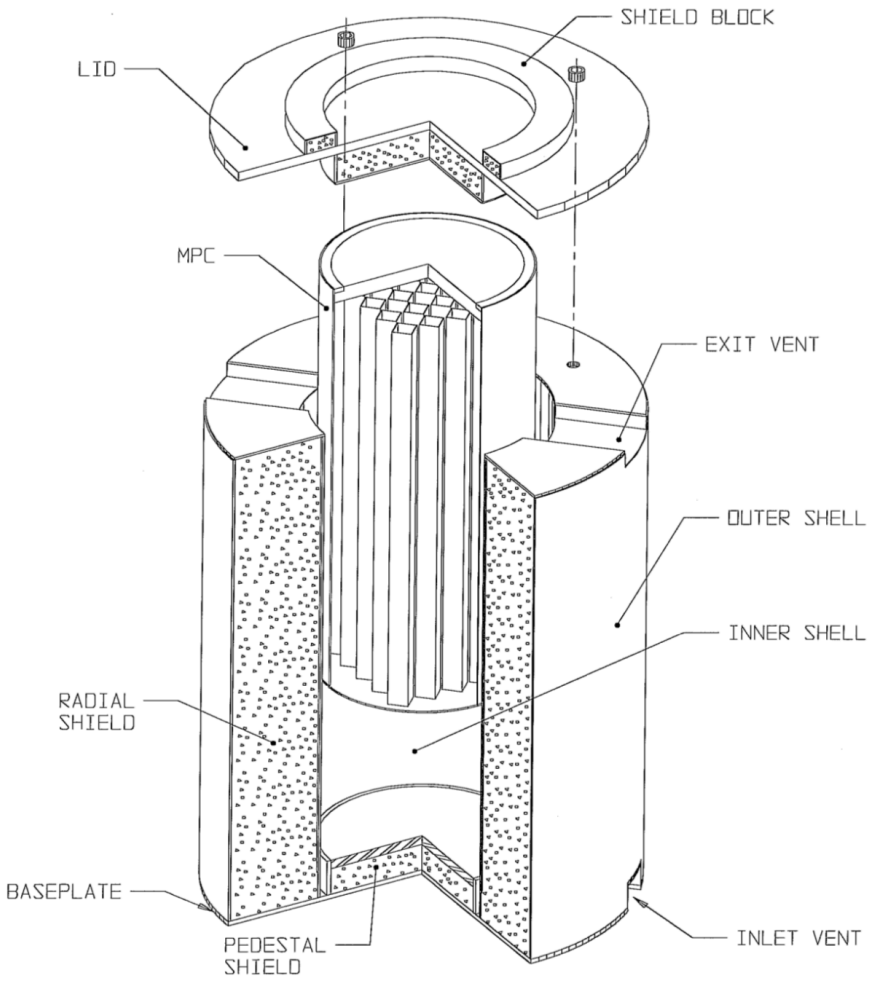

Figure 2-1. The Holtec HI-STORM 100 spent fuel cask system is designed to protect fuel, transfer decay heat to the environment, prevent proliferation of nuclear material, and attenuate radiation [32]. The MPC is seen partially inserted into the steel and concrete overpack. Current designs of the HI-STORM 100 do not use the inner shell and, therefore, the inner shield is not modeled in MCNP.

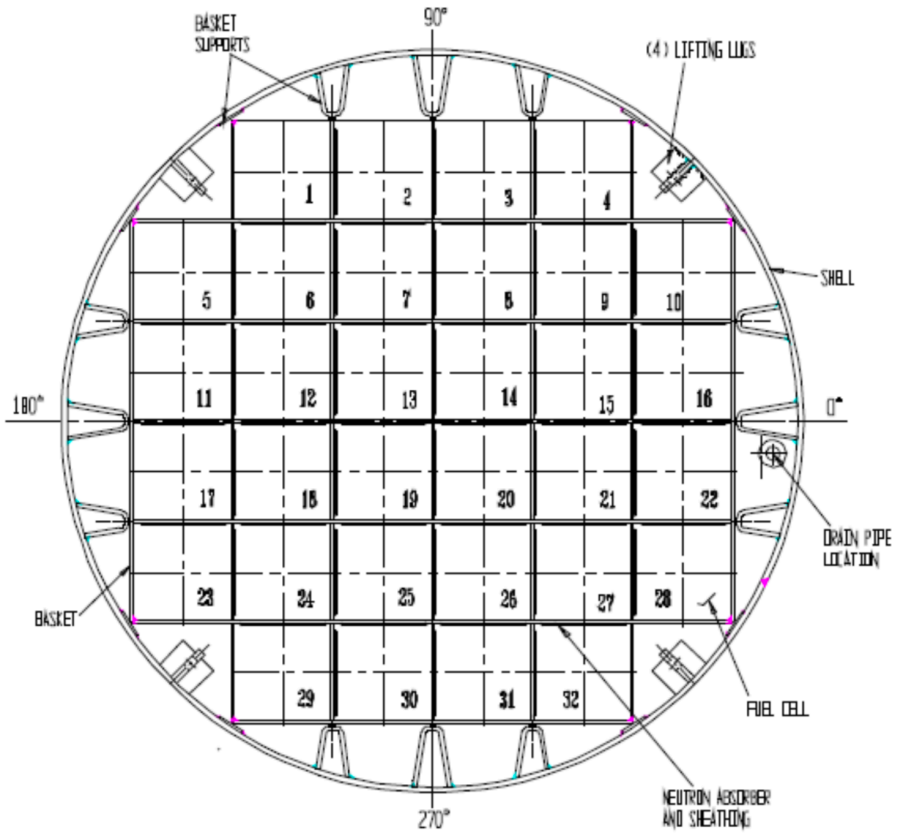

Figure 2-2. A cross section view of the multi-purpose canister. While there are multiple designs which accommodate different amounts of fuel, the MPC-32 is chosen for this work [32]. The MPC-32 is capable of holding 32 fuel bundles, one bundle in each square lattice element. The fuel basket and cylindrical wall of the MPC are made using stainless steel 304 and the canister is sealed by welding a baseplate to the bottom and a lid and closure ring to the top of the cylinder respectively.

the top-down cross section view of the MPC. Each cell in the honeycomb structure houses a single fuel bundle.

Power plant workers must be protected from the radiation produced by spent nuclear fuel rods, hence opening a sealed MPC is an expensive and potentially dangerous task. Therefore, alternative methods are being explored to ensure the content and integrity of fuel components which do not require opening a cask. A sample of these techniques includes neutron spectroscopy, deduction of interior structure based on exterior dose rates, and neutron based computer tomography which were previously discussed in detail

in Section 1.3. Each of these techniques relies on simulations using various radiation source definitions, virtual detectors, and simulated cask designs to determine specific quantities related to the neutron flux within the spent fuel cask. The key metric of this work is the interior neutron flux spatial distribution of the HI-STORM 100 spent fuel cask, as this quantity is shared among research in spent fuel casks. Clearly, simulation tools have become an important part of investigating the efficacy of a nondestructive evaluation technique, and ensuring the accuracy of these results is even more important since experimental data associated with the techniques is limited.

2.1 Description of Detailed Model

The MPC and overpack are modeled using the MCNP simulation code to determine the simulated interior neutron flux spatial distribution averaged over the height of the cask as a function of radial distance from the centerline. Figures 2-3 and 2-4 show, respectively, a side view and cross section of the cask geometry simulated in MCNP. This model is called the "detailed model" throughout this work and models the geometry of the cask down to the individual fuel rod level. Each fuel rod acts as a source term for neutrons produced from spontaneous fission and (α, n) reactions.

Figure 2-5 shows a single fuel cell cross section from the detailed model. The fuel cell contains two neutron absorbing pads composed of boron-carbide and aluminum, 264 fuel rods with zircalloy cladding and 25 water rods representing instrumentation. Fuel rod composition is determined using data from the Next Generation Safeguards Initiative which analyzed the composition of Westinghouse 17x17 fuel bundles with various degrees of initial ^{235}U enrichment and burn-up values [34]. This work investigates fuel with an initial enrichment of 3% ^{235}U and a burn-up value of 30 GWd/MTU. The composition of each individual fuel rod is unique, since fission fragment distribution is probabilistic, which introduces variance in the local neutron flux. These variations in fuel rod composition could influence the flux and potentially hide salient physics. Identifying and explaining salient physics is a goal of this work. Therefore, an average fuel rod composition is

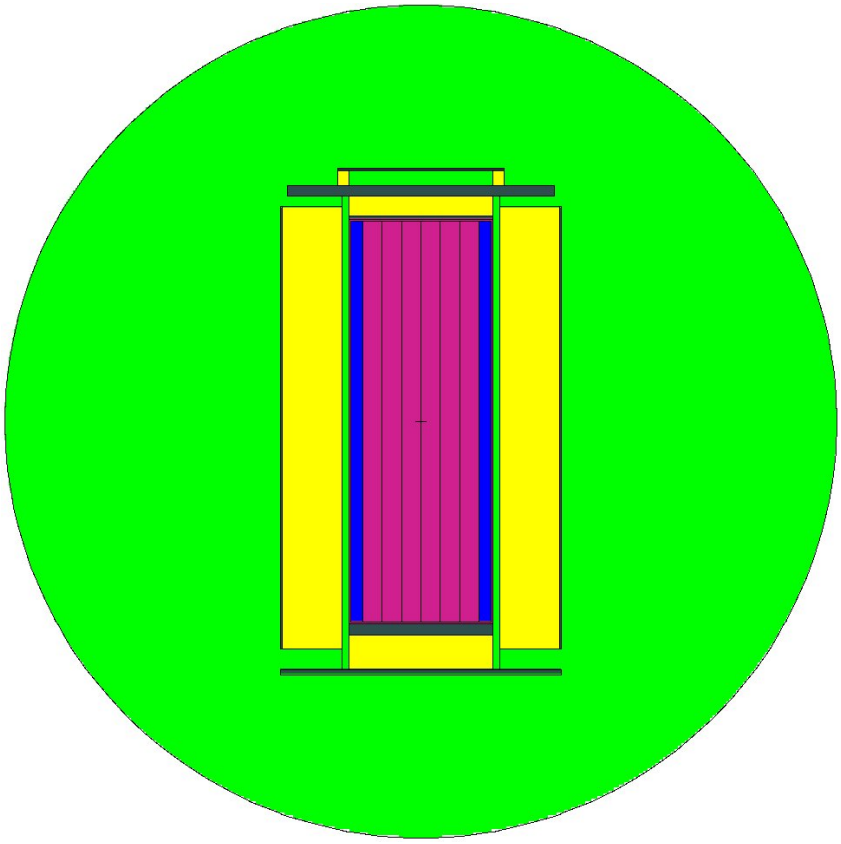

Figure 2-3. The side view of the HI-STORM 100 spent fuel cask (canister and overpack) modeled in MCNP. This is referred to as the detailed model.

523 determined based on the mass of each isotope present in a single spent fuel bundle in order
524 to more clearly investigate the effects of geometry, detail, and non-fuel materials without
525 influence from loading patterns of specific fuel rods.

526 The associated intrinsic neutron source is included via an MCNP neutron source
527 definition. This definition is found using the ORIGEN-S 0-dimensional irradiation and
528 decay code supplied with the SCALE package from Oak Ridge National Laboratory [35].
529 The neutron energy spectrum associated with the intrinsic source is shown in Fig. 2-6.
530 The source spectrum results from spontaneous fission of isotopes in the fuel (such as ^{252}Cf)
531 and (α,n) reactions occurring in the irradiated fuel.

532 Fig. 2-7 depicts the height-averaged scalar neutron flux as a function of radial
533 position within the HI-STORM 100 spent fuel cask predicted using MCNP. The color

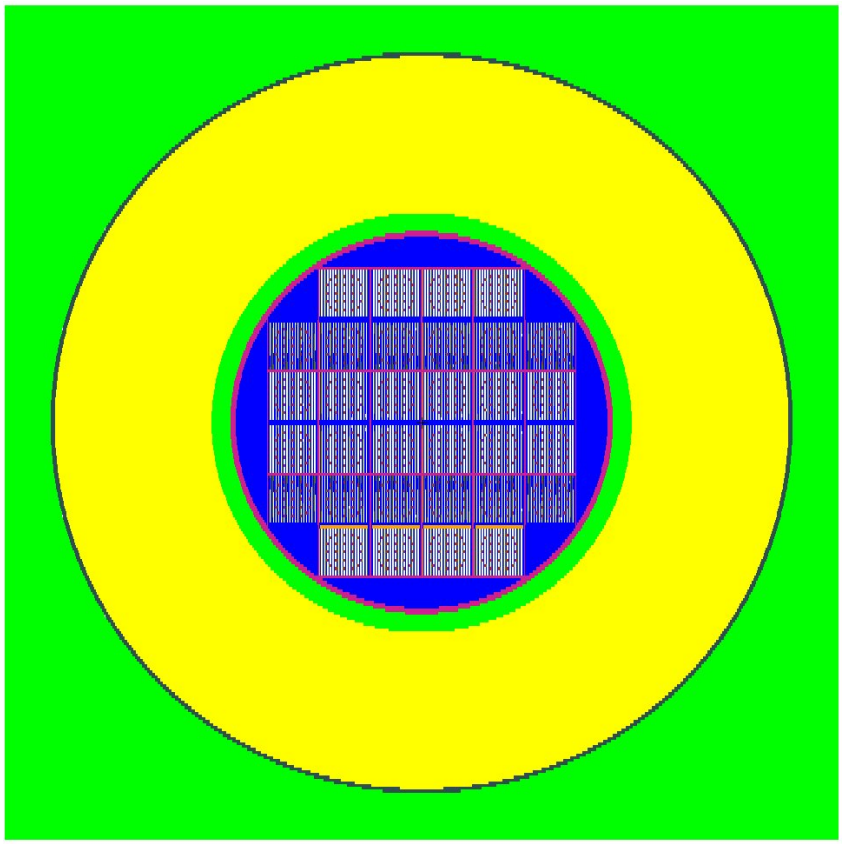

Figure 2-4. The top view of the HI-STORM 100 spent fuel cask modeled in MCNP. This view shows the fuel arrangement of the detailed model. This image shows the extent of geometric details which range from millimeters to meters.

of the line is related to the material through which the neutron flux is being simulated: fuel is green (the entire area interior to the MPC is considered the fuel region), MPC is blue, air is yellow, concrete is red, and carbon steel is black. The vertical lines designate interfaces between material boundaries; green is the interface between the fuel region and MPC, blue is the interface between the MPC and dry air, yellow is the interface between air and the concrete annulus, red is the interface between concrete and carbon steel, and black is exterior face of the cast. Figure 2-7 shows about half (54%) of the neutron flux is attenuated in the fuel region, and the concrete further reduces the flux by 39%. This result is intuitively sensible: the fuel region is comparatively dense and contains neutron-absorbing materials (e.g., boron), while the thick concrete overpack region is

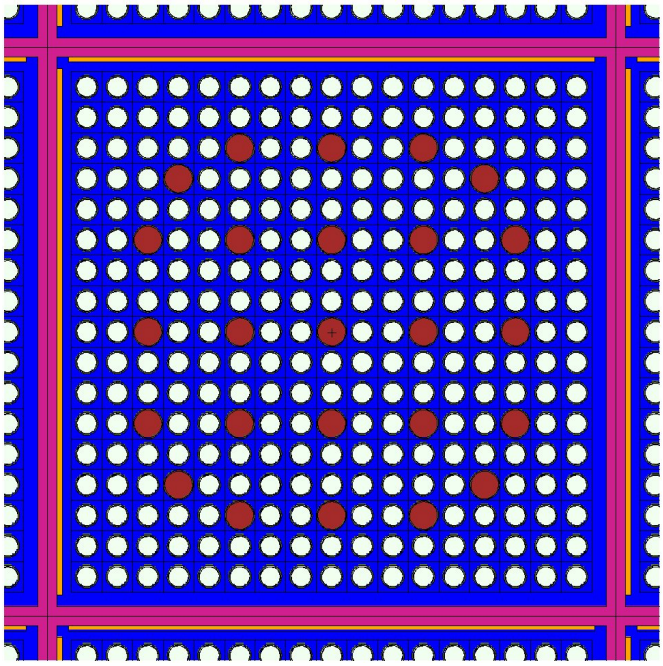

Figure 2-5. The zoomed in image of a single fuel cell cross section in the detailed model. There are neutron absorbing pads (orange rectangles) placed along the interior left and upper faces of the fuel basket (pink regions). Fuel rods (small white circles) include a fuel region, helium gap, and cladding, the helium gap and cladding are not visible in the figure. The larger red circles are the cross sectional view of water cylinders which represent instruments used for monitoring the safety of the HI-STORM 100 spent fuel cask system.

composed principally of highly thermalizing isotopes (e.g., hydrogen). Together, these processes are indicative of the observed dramatic reduction in neutron flux throughout the cask. However, advancing beyond intuition requires definitive answers to a variety of additional questions, namely:

1. Are the results correct?
2. Could a mistake have been made in the simulation input?
3. Was an assumption made that neglected important physics?
4. Does the problem include physics or exist in a physical regime outside the viability of the simulated tool used?

While corroborating simulation results with intuition is qualitatively valuable, quantitative or semi-quantitative assessments and their associated effects on confidence in simulation

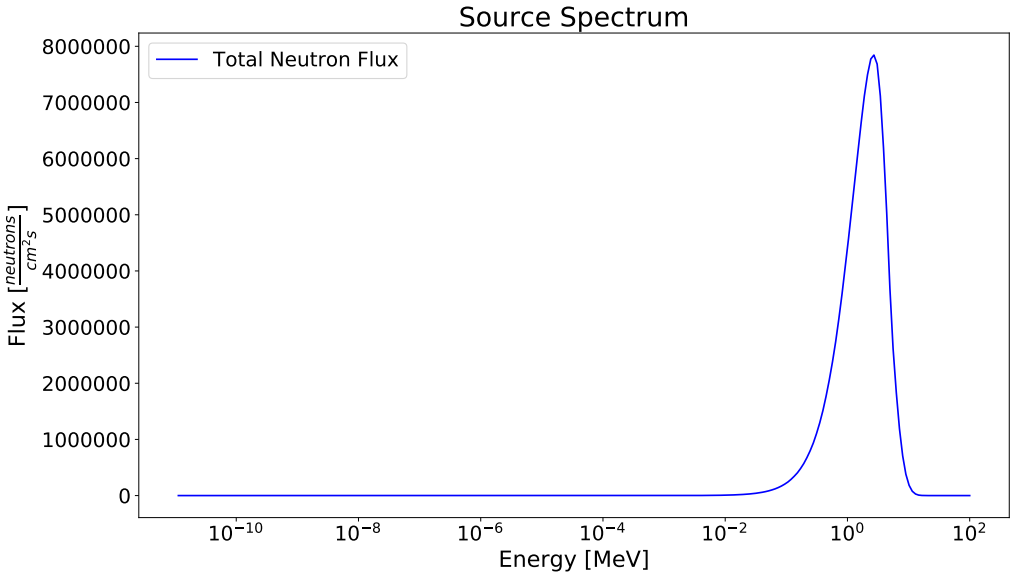

Figure 2-6. The source spectrum used in MCNP simulations. The spectrum is a result of spontaneous fission and (α, n) reactions.

results demands that the preceding questions be comprehensively addressed. The purpose of this work is to answer these questions by 1) identifying key features of the neutron flux spatial distribution as simulated in the detailed model, 2) developing simple physical models to determine the cause of each feature, and 3) gain confidence in the accuracy of the solution and inerrancy of the simulation process. In order to identify features in the neutron flux, each material region in the spent fuel cask is analyzed briefly.

2.2 Mathematical Model Choice

In the interest of constructing a complementary analytic representation of the neutron population behavior within the cask fuel region, inspection of the various features appearing in Figs. 2-1 and suggests several modeling simplifications.

- Aside from various isotope production and depletion processes featuring characteristic time scales spanning weeks to years, the spent fuel cask is essentially a static object. It is therefore assumed that the analytical representation of the cask is entirely time-independent (hereafter referred to as "static").

- The neutron energy spectrum within the fuel region is essentially "fast"; that is, it principally exists at fission neutron energies (i.e., 1-2 MeV) with minimal

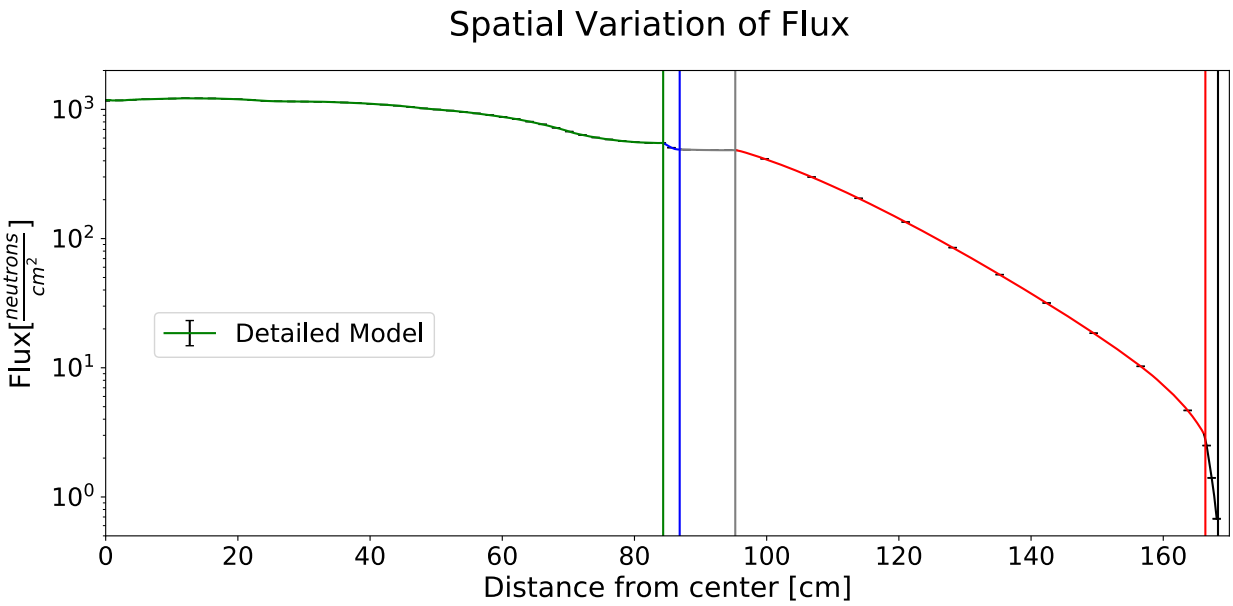

Figure 2-7. The interior neutron flux spatial distribution of the simulated HI-STORM 100 spent fuel cask. The vertical lines represent interfaces between material regions.

thermalization. As such, the analytical model used to characterize the cask fuel region is taken be approximately monoenergetic.

- Owing to the high hydrogen content in the concrete annulus, the energy spectrum can be represented with two energy groups (one thermal and one fast). An analytic model characterizing the neutron transport in concrete is assumed to require two energy groups.

As a consequence of these observations and associated simplifications, a static, monoenergetic balance law model is used to characterize the neutron population information within the cask fuel region.

2.2.1 Fuel Region

The fuel region of the HI-STORM 100 spent fuel cask features various materials including spent UO_2 nuclear fuel, a stainless steel basket, boron-containing neutron absorbing pads, and helium backfill. The geometric configuration of these materials is highly complex, as depicted in Fig. 2-1. Unfortunately, a single mathematical model capable of describing the neutron flux in the fuel region would not be tractable. Therefore, a simplified model must be developed using assumptions and approximations derived from

physics occurring in the model. In order to identify appropriate simplification, the energy spectrum and angular distribution of the neutron flux and cross section data of various materials are analyzed at various locations in the fuel region.

Figure 2-8 shows the energy spectrum of the neutron flux throughout the spent fuel cask. These plots show the neutron flux has little variation throughout the fuel region. This is a result of evenly distributing fuel rods through the fuel region. Further, the lack of thermalizing materials in the fuel cask means there is little change in the neutron spectrum. Therefore, it can be assumed that energy dependence of the neutrons can be handled uniformly throughout the fuel region. This is a very helpful assumption that allows for uniform treatment of material properties throughout the fuel region with respect to energy. Unfortunately, there have been no assumptions concerning how to handle neutron energy-dependence at this point, (e.g., is a monoenergetic method appropriate, or will a different model be require?).

Analysis of the energy spectrum will determine how to best handle energy-dependence. The percent of neutrons above 10keV varies between ~78% at inner radius values to ~71% at the edge of the fuel region as shown in Figs. 2-8a-2-8h. A monoenergetic handling of the energy-dependence can be assumed since the majority of neutrons have energies between 10keV and 10MeV, using an appropriate group weighting spectrum described by Bell and Glasstone [36]. After choosing a method for handing energy-dependence, it becomes necessary to determine a method for handling directional-dependence of the neutron flux.

Figure 2-9 shows the angular distribution of the flux 0.5cm from the centerline (Fig. 2-9a) and at the edge of the fuel region (Fig. 2-9b). The angular distribution was tallied at these locations to capture the two extents of the angular flux. A perfectly isotropic flux would be a horizontal line with zero slope. If half of the neutron population is traveling in either direction (inward and outward), then the neutron flux can be approximated as isotropic with the understanding that deviations from isotropy will lead to errors in

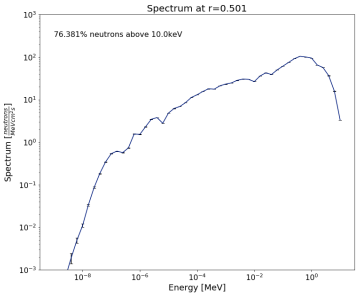
Spectrum at r=0.501
76.381% neutrons above 10.0keV
Spectrum [neutrons/MeV/cm²]
Energy [MeV]

(a)

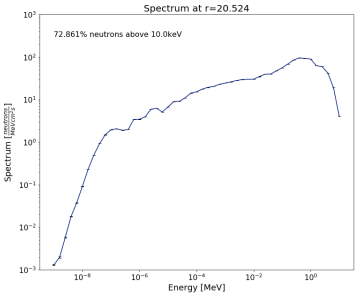
Spectrum at r=20.524
72.861% neutrons above 10.0keV
Spectrum [neutrons/MeV/cm²]
Energy [MeV]

(b)

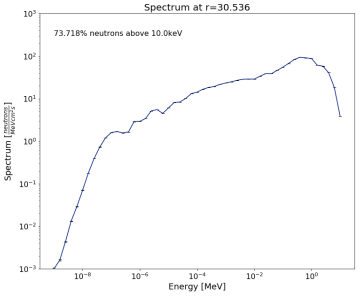
Spectrum at r=30.536
73.718% neutrons above 10.0keV
Spectrum [neutrons/MeV/cm²]
Energy [MeV]

(c)

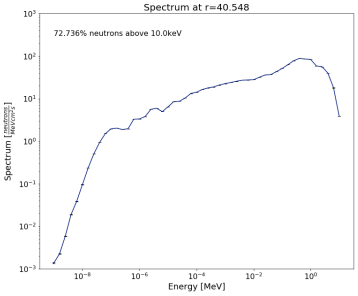
Spectrum at r=40.548
72.736% neutrons above 10.0keV
Spectrum [neutrons/MeV/cm²]
Energy [MeV]

(d)

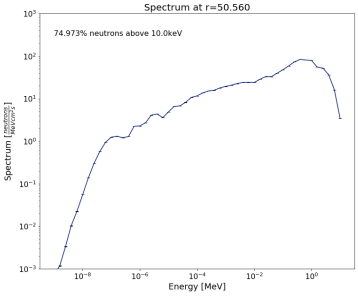
Spectrum at r=50.560
74.973% neutrons above 10.0keV
Spectrum [neutrons/MeV/cm²]
Energy [MeV]

(e)

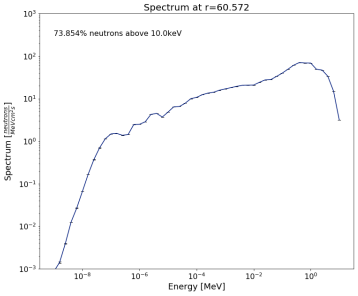
Spectrum at r=60.572
73.854% neutrons above 10.0keV
Spectrum [neutrons/MeV/cm²]
Energy [MeV]

(f)

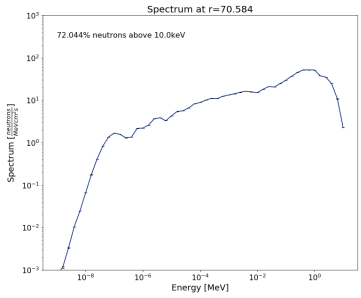

(g)

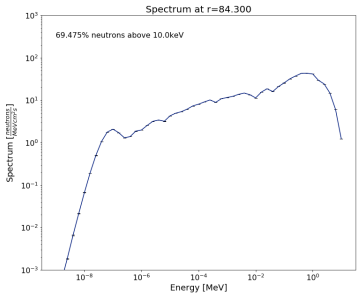

(h)

Figure 2-8. Energy spectrum of the neutron flux at various locations in the MPC where fuel rods are stored.

the results. Figure 2-9a shows the neutron flux is slightly inward-peaked 0.5cm from the centerline with 50.278% of all neutrons traveling toward the centerline. This indicates the flux can be approximated as isotropic near the centerline, a perfectly isotropic flux would have 50% of neutrons scattering toward the center of the fuel region. The flux at the outer edge has an outward peaked flux as shown in Fig. 2-9b. This is because the neutron population density is high in the fuel region, since the source of neutrons is in the fuel region, and neutrons are diffusing, or leaking, out of the fuel region where the neutron population density is lower. The percent of neutrons traveling outward from the fuel region 57.290% at the surface of the fuel region. While, the angular distribution in Fig. 2-9b shows the neutrons are slightly forward peaked, the angular distribution of the neutron flux deviates from isotropic by only $\sim$7%, thus, can be approximated as isotropic with the understanding that this approximation may lead to some disagreement between analytic and computational results.

Figure 2-10 shows the mean-free-path (MFP) of each of the materials in the fuel region. The MFP is the average distance between neutron interactions in a material. Figure 2-10 shows the MFP in the fuel (blue), cladding (orange), helium (green), stainless

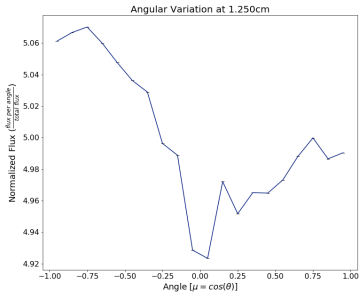

(a)

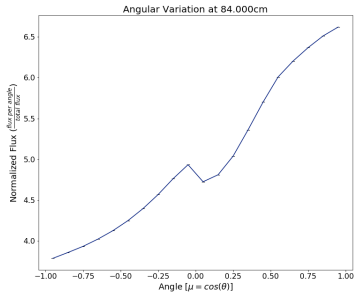

(b)

Figure 2-9. Angular distribution of the neutron flux at 2-9a 0.50 cm and at 2-9b the inner surface of the MPC (84.3 cm) from the centerline of the fuel cask.

steel (red), and neutron absorbing material (purple). The source flux is also shown in grey to identify which energy regions are most important (i.e., energy regions where the source flux is higher are more important). Assessing the MFP of each material helps to identify other assumptions and approximations that aid in determine the appropriate mathematical model to represent the neutron flux. The MFP of helium is about 1km where the source flux is most intense near 1MeV. The thickest region of helium occurs between the fuel cells and edge of the fuel region and is on the order of 10cm thick. The MFP is approximately two orders of magnitude larger, meaning there will be a negligible number of neutrons interacting in helium. The first material assumption is that helium outside of the fuel cells can be neglected. The remaining materials have a MFP of approximately 1cm at 1MeV. These materials show up in the fuel region on the same order, therefore, the remaining materials cannot be neglected. However, since these materials are evenly distributed (i.e., the materials exist throughout the fuel region and not just at a single location) and since the remaining materials have similar MFP's, a homogenization technique can be used to approximated the geometry in the fuel region.

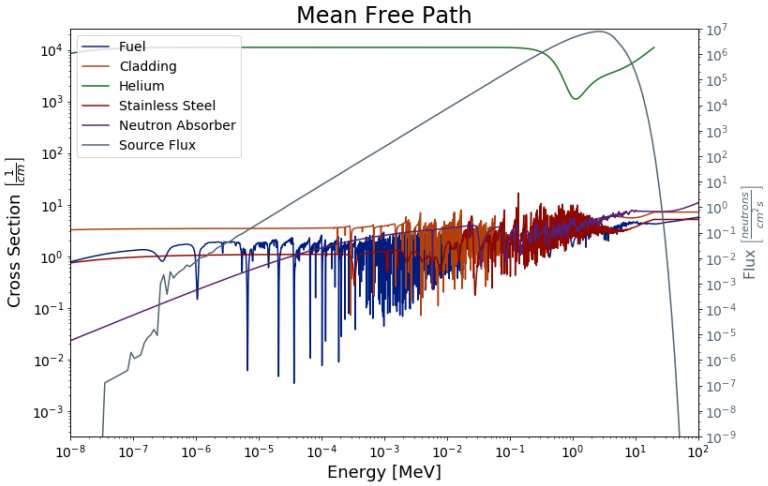

Figure 2-10. The mean-free-path, or distance between interactions, of the materials in the fuel region. The source flux is provided in order to identify energy ranges of greater importance.

A cylinder shaped homogenous fuel material is made based on the weight ratio of each material in the fuel region. The volume of the homogenous cylinder of fuel material is determined to preserve the volume from the 32 original fuel cells, and the radius of the cylinder is approximately 75cm. The volume around the cylinder of homogenous fuel is treated as a vacuum in the mathematical model. The radius of the homogenized fuel is about two orders of magnitude greater than the MFP of the materials used in the fuel region (e.q., $\sim$100cm radius of fuel $>>$ $\sim$1cm MFP). Hence, the diffusion equation is an appropriate model since the fuel material is much thicker than the neutron's MFP. Therefore, the monoenergetic diffusion equation is an appropriate mathematical model to represent the neutron flux in the fuel region, given the previous identified assumptions and approximations derived from physical properties of materials in the fuel region.

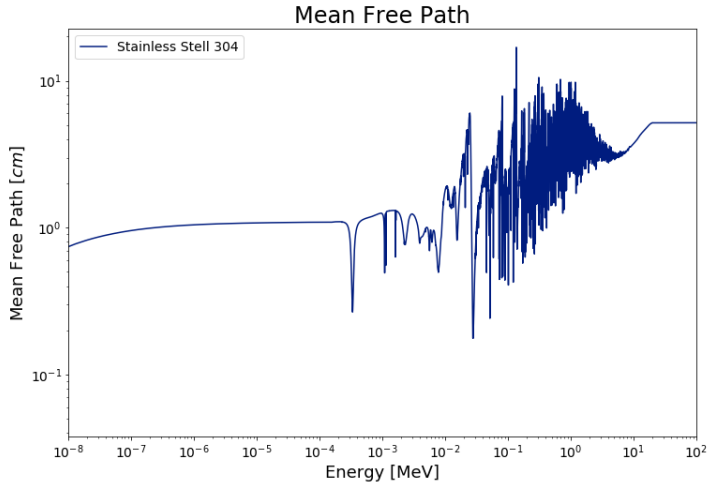

Figure 2-11. The mean-free-path of neutrons in stainless steel 304.

A monoenergetic diffusion approximation is an appropriate choice of an analytic model for the fuel region, however, that may not be the case for other materials in the cask. It is important to identify how the flux behaves in the remaining materials of the fuel cask and to identify appropriate models.

2.2.2 Stainless Steel MPC

The MPC encompasses the fuel area in a 2.5cm thick stainless steel 304 cylindrical container. Figure 2-11 shows the MFP in stainless steel 304. The most important thing to notice from the figure is that the MFP is on a similar order of magnitude as the thickness of the MPC. The diffusion equation is not an appropriate model when a material's thickness is fewer than a couple MFP's thick. Therefore, the diffusion approximation is unlikely to be an appropriate mathematical model. Instead, the multigroup discrete ordinates equation is a better approximation in this situation.

The number of energy groups and angles required to adequately model neutron transport in the stainless steel is still needed. Analyzing the energy spectrum at the interior and exterior surface of the MPC aid in finding an appropriate number of energy groups. Figure 2-12 shows the neutron energy spectrum at the interior surface (Fig. 2-12a) and exterior surface (Fig. 2-12b) of the MPC. At the interior surface of the MPC, the neutron flux is ∼70% above 10keV and a single energy model would be appropriate. This would be preferable since the group structure in the MPC would match the energy group boundaries in the fuel region. However, the number of slow neutrons increases though the thickness of the MPC, and Fig. 2-12b shows that ∼59% of neutrons are above 10keV. Hence, a two group analytic model is preferable.

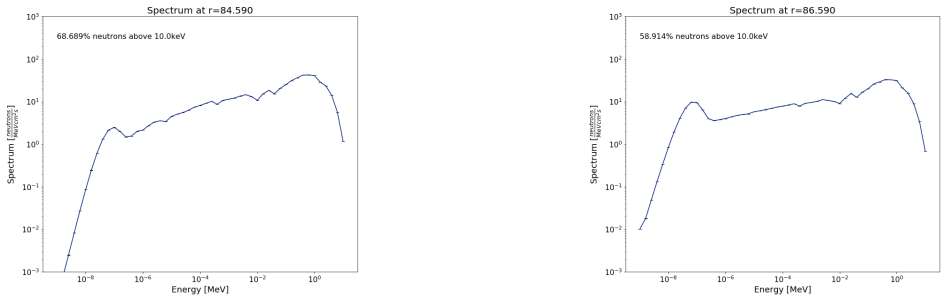

(a) (b)

Figure 2-12. The neutron energy spectrum at a) 84.6cm and b) 86.6cm in the stainless steel MPC.

Analysis of the angular distribution (Fig. 2-13) helps to determine the number of angles to use in the multigroup discrete ordinates approximation. Figure 2-13a is the angular distribution of the flux at the interior surface of the MPC. Approximately 57% of the neutrons are forward scattering at this point in the MPC and Fig. 2-13b shows that the number of forward scattered neutrons is relatively similar (∼56%). In the fuel region, the flux is considered isotropic even though over half of the neutrons are

traveling away from the centerline near the outer surface of the cask. This is an acceptable approximation since there exists location in the fuel region that are closer to isotropic. However, the neutron flux in the stainless steel is only forward-pointed, which alludes to using two angles to approximate the neutron flux. Finally, the multigroup discrete ordinates approximation with two energy groups and two angles is chosen to model neutron transport in the stainless steel.

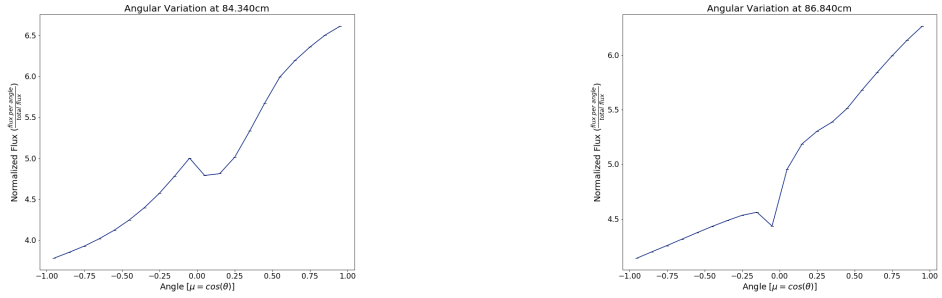

(a) (b)

Figure 2-13. The neutron angular distribution at the a) inner surface and b) outer surface of the MPC.

2.2.3 Dry Air Gap

Surrounding the MPC is a gap of dry air for heat removal from the fuel. Figure 2-14 shows the mean free path of neutrons in dry air. The MFP is two orders of magnitude larger than the thickness of the air gap (∼10cm). Meaning, the air gap can be treated as a vacuum and there is no need for a mathematical model in this region.

2.2.4 Concrete Annulus

The 71.12cm thick concrete annulus provides nearly half the neutron shielding capabilities in the spent fuel cask due to scattering on hydrogen. Following a similar method as before, the MFP of neutrons in concrete are investigated. Concrete, being a thermalizing material, is expected to change the neutron energy spectrum through

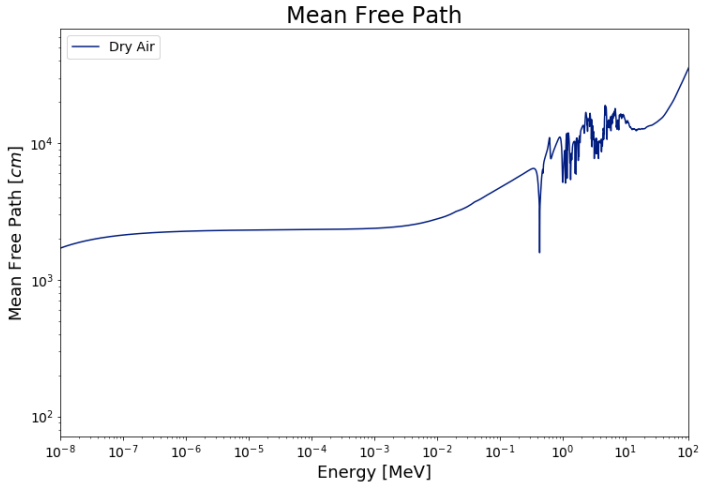

Figure 2-14. The mean-free-path of neutrons in the air gap. The low density of gaseous air lead to a high MFP. The air gap can be treated as a streaming region since the MFP is much larger than the thickness of the air gap.

down-scattering neutrons, so both fast and thermal energies need to be taken into account when analyzing Fig. 2-15. At higher energies, 1MeV, the concrete is about 7 MFP's thick. Therefore, diffusion may not be an appropriate model for these energies of neutrons. However, at lower energies, 1eV, the concrete is about 35 MFP's thick. At lower energies, the diffusion approximation is an appropriate model. Overall, analysis of Fig. 2-15 would indicate that a multigroup discrete ordinates approximation would be better suited as an analytic model in the entire concrete. Further investigation of the neutron energy spectrum and angular distribution will aid in solidifying a model choice.

The energy spectrum does change significantly over the thickness of the concrete annuls. Figure 2-16a shows the neutron energy spectrum at the inside surface of the concrete annulus. The neutron flux is ∼53% above 10keV at the innermost surface of the concrete. The neutron flux is quickly thermalized and less than a third of the neutron flux

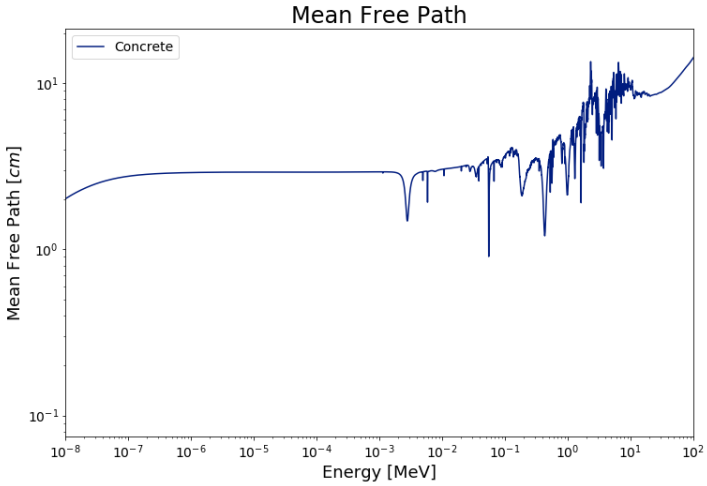

Figure 2-15. The mean-free-path of neutrons in the concrete annulus.

is above 10keV after the neutrons have traveled ten centimeters into the concrete (Fig. 2-16b). At the exiting surface, less than 6% of the neutrons remain above 10keV as shown in Fig. 2-16h. The large change in neutron energies means more than one energy will be required to model transport in concrete. The shape of the flux shows the presence of two local maxima in the neutron spectrum that occur throughout the concrete region, one near 1MeV and the other near 0.1eV. Therefore, a two energy group model is expected to be adequate. Analysis of the angular distribution will indicate the number of angles necessary for the multigroup discrete ordinates model.

Figure 2-17 show the angular distribution at the entering and exiting surfaces of the concrete annulus. Analysis of the angular distribution shows the neutron flux is forward-peaked with ∼55% of the neutrons traveling outward at the inner surface of the concrete annulus. At the exiting surface, ∼68% of the neutrons are traveling outward. This results confirms the model choice of the multigroup discrete ordinates approximation. Further, two angles are adequate to describe the flux to a first-order-approximation.

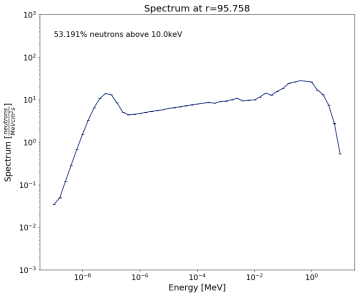
Spectrum at r=95.758
53.191% neutrons above 10.0keV
Spectrum [neutrons / MeV/cm²]
Energy [MeV]

(a)

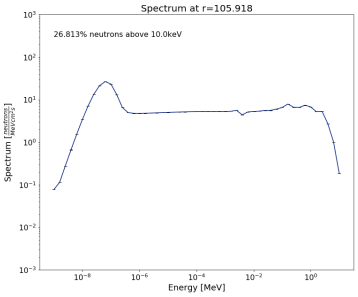
Spectrum at r=105.918
26.813% neutrons above 10.0keV
Spectrum [neutrons / MeV/cm²]
Energy [MeV]

(b)

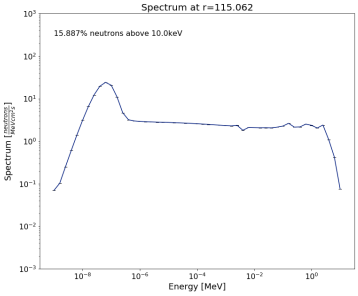
Spectrum at r=115.062
15.887% neutrons above 10.0keV
Spectrum [neutrons / MeV/cm²]
Energy [MeV]

(c)

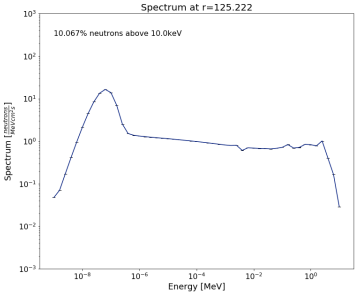
Spectrum at r=125.222
10.067% neutrons above 10.0keV
Spectrum [neutrons / MeV/cm²]
Energy [MeV]

(d)

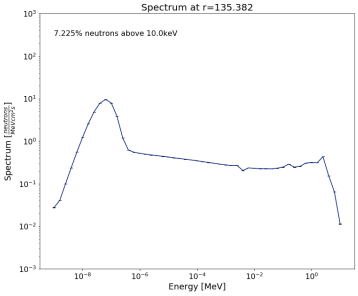
Spectrum at r=135.382
7.225% neutrons above 10.0keV
Spectrum [neutrons / MeV/cm²]
Energy [MeV]

(e)

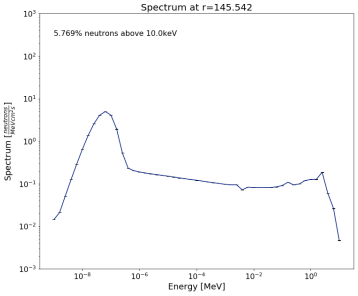
Spectrum at r=145.542
5.769% neutrons above 10.0keV
Spectrum [neutrons / MeV/cm²]
Energy [MeV]

(f)

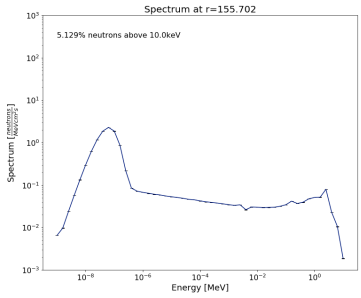

(g)

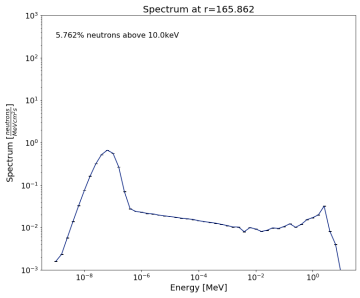

(h)

Figure 2-16. Energy spectrum of neutrons throughout the concrete annulus.

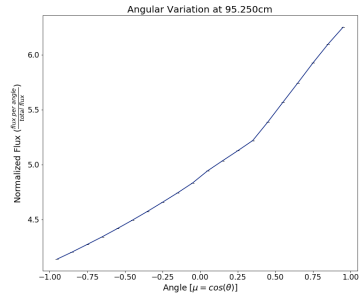

(a)

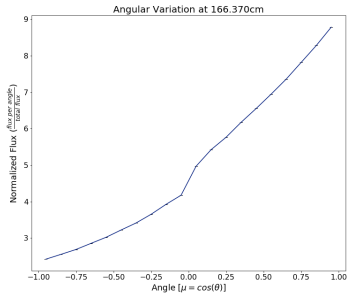

(b)

Figure 2-17. The angular distribution of the neutron flux at a) the inner surface (95.25cm) and the b) outer surface (166.37cm) of the concrete annulus.

2.2.5 Carbon Steel Outer Shell

The 1.905cm thick carbon steel shell is the final material being analyzed in the spent fuel cask. Using a similar analysis as with previous materials, the MFP is compared to the thickness of the steel shell to aid in determining a mathematical model. Figure 2-18 shows the MFP of neutrons in carbon steel. The most probable energy of neutrons leaving entering the carbon steel shell is about 0.1MeV, shown in Fig. 2-16h. Using this information, the most probable MFP of neutrons in the carbon steel shell is ∼1cm. This is

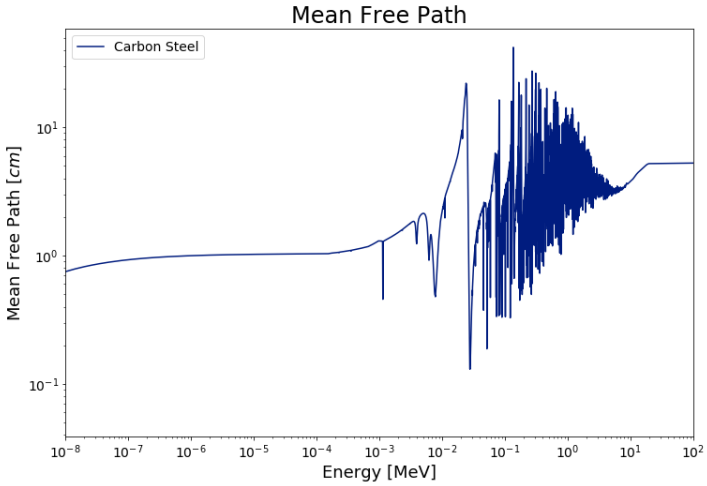

Figure 2-18. The mean-free-path of neutrons in carbon steel.

on the order of the magnitude of the carbon steel shell thickness. Therefore, the diffusion equation is likely a poor choice of mathematical model and the multigroup discrete ordinates equation is likely a better choice.

Figure 2-19 shows the energy spectrum at the inner surface (Fig. 2-19a) and outer surface (Fig. 2-19b). A small number of neutrons are are bred in carbon steel resulting in the growing number of neutrons above 10keV. For this reason, two energy groups should be used to model the neutron flux in the carbon steel.

Finally, the angular distribution graphs of the neutron flux entering the carbon steel (Fig. 2-20a) and leaving the carbon steel shell (Fig. 2-20b) show the neutron flux is forward peaked. In fact, at the inner carbon steel surface ∼68% of the flux is traveling outward and that fraction increases to ∼97% of neutrons traveling outward at the exiting surface of the cask. Nearly all of the neutrons are traveling away from the cask because the cask is placed in dry air. As shown previously, the MFP of neutrons in dry air is large, greater than 1km, resulting in a small number of neutrons returning to the cask after

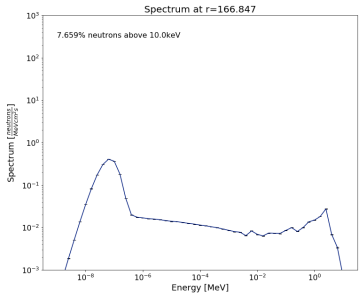

(a)

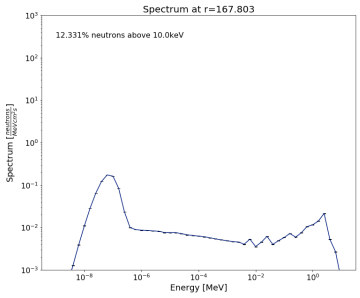

(b)

Figure 2-19. The neutron energy spectrum near the a) inner surface (166.847cm) and the b) outer surface (167.803cm) of the carbon steel shell. The two peaks in each figure allude to a two energy group model.

leaving. The small number of returning neutrons provides boundary condition information for the final model. Therefore, the outermost boundary of the spent fuel cask can be treated as non-reentrant. Further, two angular groups are capable of approximating the flux since the distribution is strongly preferential in a forward direction.

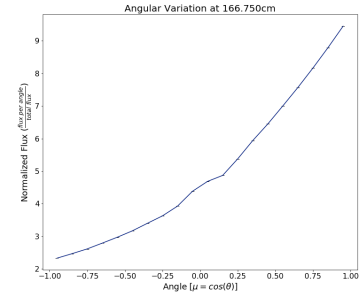

(a)

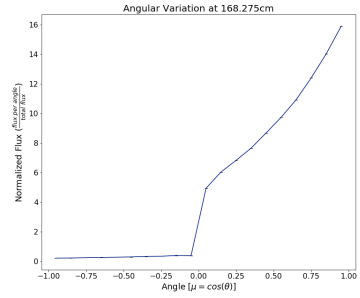

(b)

Figure 2-20. The angular distribution of the neutron flux at the a) inner surface and b) outer surface of the carbon steel shell. Since the flux is heavily forward-pointed, two directions can be used to model the flux.

By no means are the previous choices in analytic models meant to be the most exhaustive means of describing the neutron flux in each material. Rather, choices were made in order to keep the models as simplistic as possible while capturing the physics of the spent fuel cask in an attempt to highlight inherent phenomenon in the problem. As will be seen during the sensitivity analysis portion of the work, even these simplistic models yield complex sensitivity results. Therefore, identifying any physical meaning using the analytic models becomes challenging, if possible, even when using very simple models. While the mathematical models have been chosen, the geometry which each will be solved in has yet to be determined. Discussion of the geometry will be handled in Sec. **??**.

2.3 Identification of Features

"Features" are locations in the simulated neutron flux spatial distribution shown in Fig. 2-7 which appear to be the result of a physical process. Using a reduced complexity analytic or computational model to reproduce a feature yields two benefits: 1) the physical process that generates the feature in question is identified and, 2) confidence is gained in the accuracy of the simulation result. Confidence in the simulation result is gained when a feature is determined to be a result of an understood physical process. That is, the feature should exist in the problem, is being modeled correctly in the code, and is not a computational artifact. Ensuring agreement between simplified and complex models also corroborates the accuracy of the simulation input itself. Something as simple as inputing an incorrect area or volume would not result in a fatal error message in MCNP, but would lead to incorrect neutron flux results. The process of reproducing features using simplified analytic and computational models provides an opportunity to identify errors in the simulation input and addressing these errors leads to increased confidence in the accuracy of a simulation.

There are four features discussed in this paper which are identified as:

1. The "flat" flux region (highlighted in Fig. 2-21): The flux in this region smoothly decreases by approximately 36% even though intuition suggests the flux should increase in the fuel pins and decrease in the space between fuel pins.
2. The abrupt level-off region (highlighted in Fig. 2-22): The flux only decreases ∼3 % over the region 65 cm $\leq r \leq$ 84.1 cm from the cask centerline.
3. Periodic depressions (highlighted in Fig. 2-23): There is a ∼2% reduction in the flux near 25 cm, 50 cm, and 75 cm from the cask centerline.
4. The asymmetric flux: Figure 2-24 is a density plot of the neutron flux when looking at a center slice of the cask from above. Figure 2-25 is a contour plot to better illustrate the neutron flux asymmetry present in Fig. 2-24. The neutron flux in the upper left section (above the diagonal line) of the plot is less than the neutron flux in the lower right section (below the diagonal line) of the image. This asymmetry is most obvious at the outer edge of the fuel region.
5. The concrete flux (Fig. 2-26): The concrete region provides the second-most significant reduction in the neutron flux within the cask. Identifying the processes which attenuate radiation in this region provides evidence the overpack was modeled correctly.

The remaining chapters will discuss how the results assessment methodology is used to identify the salient physics in each of the previously identified features, as well as, how confidence is gained in the simulation results of the detailed model through sensitivity analysis. However, the next chapter will provide an in-depth background on neutron transport theory and the development of the analytic models which will be used in the analysis before we can discuss the features further.

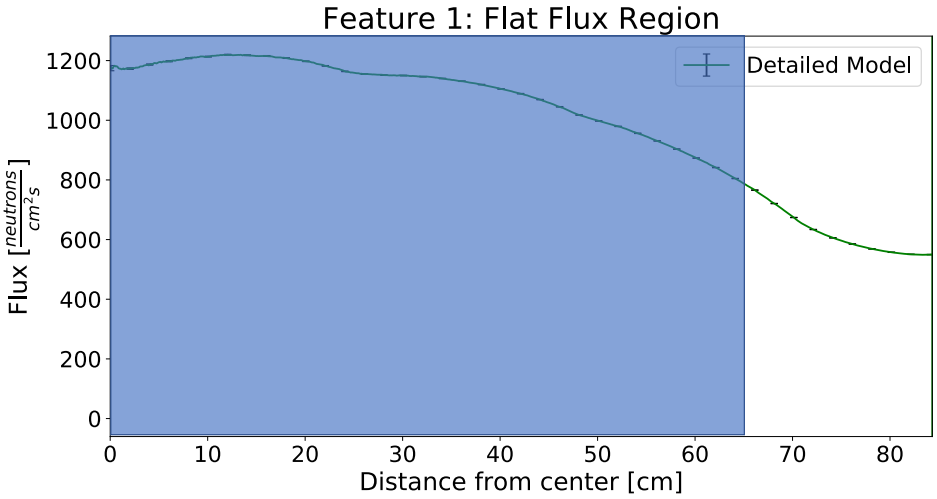

Figure 2-21. The neutron flux spatial distribution between the cask centerline and inner face of the MPC. The highlighted region is considered the flat flux region. This neutron flux is relatively flat and does not vary on the same order as the physical dimensions of materials in this region.

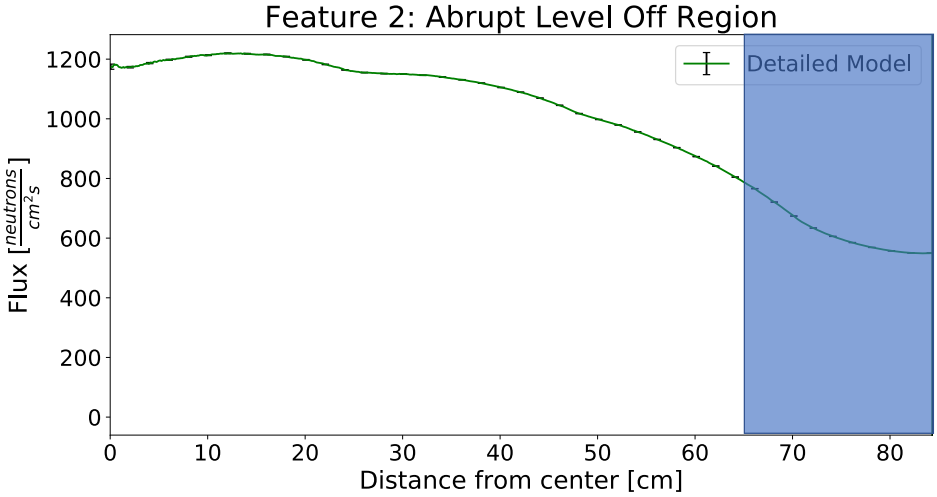

Figure 2-22. The flux stops decreasing and instead levels-off in the abrupt level-off region. The flux decreases less than 3% over the last ten centimeters before the interface between the fuel region and MPC.

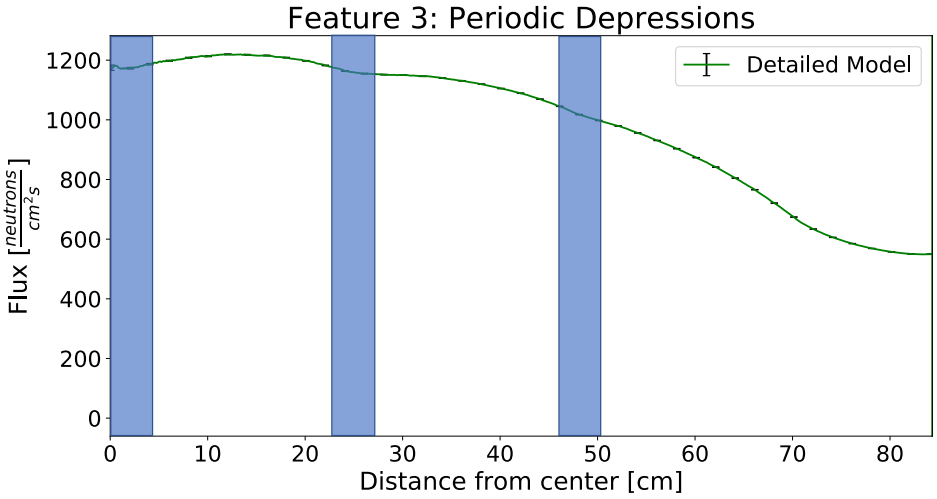

Figure 2-23. There are three depressions in the neutron flux spatial distribution located approximately 22 cm apart. The flux decreases about 2% at each depression.

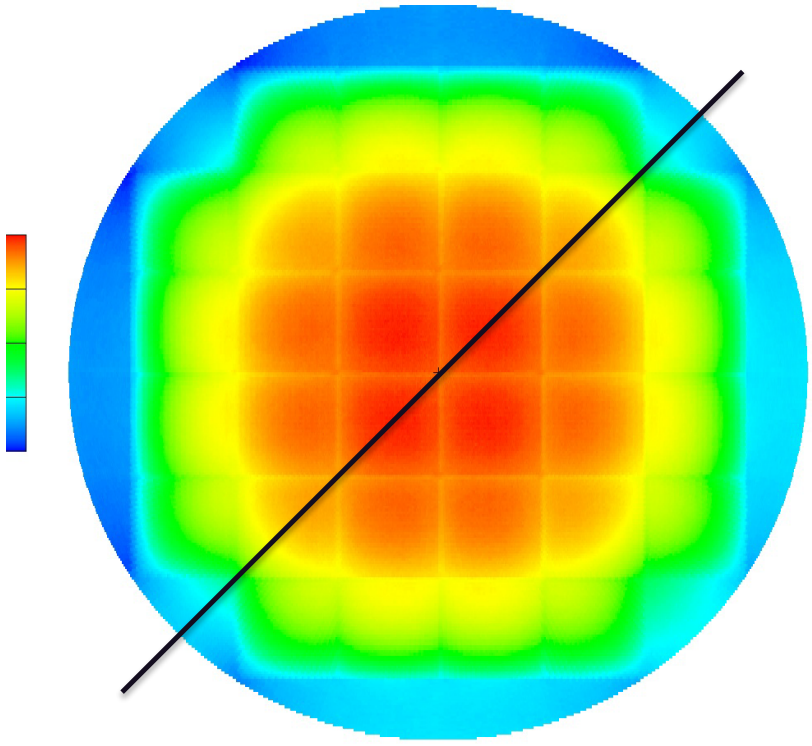

Figure 2-24. A density plot of the neutron flux at a "central slice" of the fuel cask as viewed from above. This plot shows the neutron flux is less in the upper left section than in the lower right section. The asymmetry is most evident in the blue and light blue sections at the outer radius of the figure.

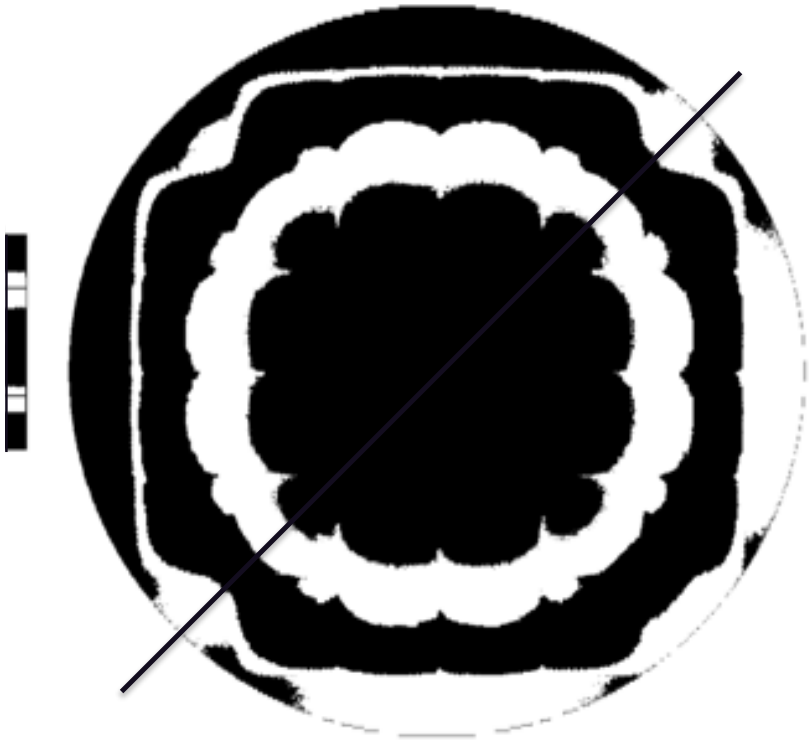

Figure 2-25. A contrast plot emphasizing the asymmetry of the flux values.

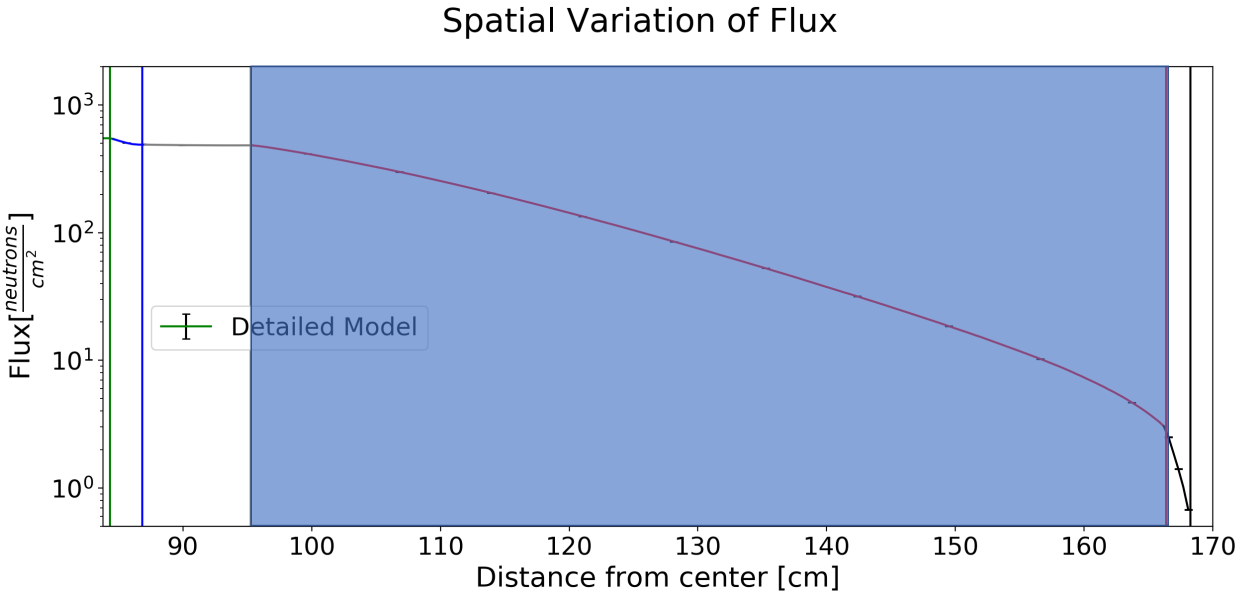

Figure 2-26. The overpack accounts for about half of the reduction to the neutron flux. The purpose of investigating this region is to determine which physical processes are responsible for the attenuation.

CHAPTER 3
THEORY

The behavior of any nuclear system is governed by the distribution of radioactive particles within the system. In the case of a system containing neutrons, the distribution of neutrons can be found by solving the neutron transport equation (NTE). The NTE is also referred to as the Boltzmann transport equation because of its similarity to Boltzmann's equation governing the kinetic theory of gas. Finding an analytic solution of the NTE for even the simplest geometries is a challenging task. Not only because the equation is an integro-differential equation defined over a seven variable phase space, but also because the solution of the NTE depends on parameters which are heavily dependent on the solution to the original equation. The NTE can be solved for the flux by applying assumptions and approximations to reduce the complexity of the equation. The NTE is derived before applying assumptions and simplifications to reduce the NTE into two, distinct tractable approximations; known as (1) the diffusion approximation and (2) the multigroup discrete ordinates equations.

Before deriving the NTE, it is important to define terms which will be used. The neutron angular density,

$$N(\boldsymbol{r}, \hat{\boldsymbol{\Omega}}, E, t),$$

describes the expected number of neutrons in the region of phase space defined by a neutron's position vector $\boldsymbol{r}$, direction of travel $\hat{\boldsymbol{\Omega}}$, and kinetic energy E at time t. It follows that the expected number of neutrons at time t in a volume element $\mathrm{d}V$ having energies in $\mathrm{d}E$ about E and directions within a narrow beam $\mathrm{d}\hat{\boldsymbol{\Omega}}$ about $\hat{\boldsymbol{\Omega}}$ can be described by

$$N(\boldsymbol{r}, \hat{\boldsymbol{\Omega}}, E, t)\,\mathrm{d}V\,\mathrm{d}\hat{\boldsymbol{\Omega}}\,\mathrm{d}E.$$

The angular flux is defined as the product of speed v and the number of neutrons,

$$\boldsymbol{\varphi}(\boldsymbol{r}, \hat{\boldsymbol{\Omega}}, E, t) = vN(\boldsymbol{r}, \hat{\boldsymbol{\Omega}}, E, t).$$

Using the angular flux, the reaction rate is defined as

$$R_x(\boldsymbol{r}, \hat{\boldsymbol{\Omega}}, E, t) = \Sigma_x(E)\boldsymbol{\varphi}(\boldsymbol{r}, \hat{\boldsymbol{\Omega}}, E, t)$$

where $R_x(\boldsymbol{r}, \hat{\boldsymbol{\Omega}}, E, t)$ is the frequency of interactions between neutrons and surrounding materials. The parameter $\Sigma_x(E)$ called the macroscopic cross section for reaction "x" (e.q., total reaction cross section, absorption cross section, scattering cross section). The macroscopic cross section describes the probability of an interaction occurring per unit length as a function of incoming neutron energy.

3.1 Derivation of the Boltzmann Transport Equation for Neutrons by Derivatives

The NTE can be derived by "following" a group of neutrons, referred to as a packet, through a material and describe how neutrons are gained or lost in time. Neutrons with energy E are lost from the packet as a result of a collision over the distance $v\Delta t$, whereas neutrons that do not interact over the distance $v\Delta t$ remain in the packet. The probability of a neutron being removed from the packet over the distance $v\Delta t$ can then be written as

$$\begin{matrix}\text{Probability of a neutron} \\ \text{being removed from the packet}\end{matrix} \equiv \Sigma_t(\boldsymbol{r}, E)v\Delta t, \tag{3-1}$$

and the probability of a neutron remaining in the packet over the distance $v\Delta t$ is defined as

$$\begin{matrix}\text{Probability of a neutron} \\ \text{remaining in the packet}\end{matrix} \equiv 1 - \Sigma_t(\boldsymbol{r}, E)v\Delta t. \tag{3-2}$$

Using 3-2, the number of neutrons remaining in the packet after traveling a small distance of $v\Delta t$ is

$$\begin{matrix}\text{Number of neutrons} \\ \text{remaining in packet}\end{matrix} \equiv N(\boldsymbol{r}, \hat{\boldsymbol{\Omega}}, E, t)[1 - \Sigma_t(\boldsymbol{r}, E)v\Delta t]\,\mathrm{d}V\,\mathrm{d}\hat{\boldsymbol{\Omega}}\,\mathrm{d}E. \tag{3-3}$$

Eqn. 3-3 adjusts the neutron population accounting for neutrons which left the packet through interactions, however, neutrons can enter the packet through two mechanisms: 1) internal neutron source or 2) by scattering from one packet into another. The number of

neutrons which enter the packet from an internal neutron source is given by

$$\begin{aligned}&\text{Number of neutrons entering}\\&\text{packet from internal sources}\end{aligned} \equiv s(\boldsymbol{r},\hat{\boldsymbol{\Omega}},E,t)\,\mathrm{d}V\,\mathrm{d}\hat{\boldsymbol{\Omega}}\,\mathrm{d}E\Delta t. \tag{3-4}$$

Neutrons can also enter the packet through scattering interactions, called inscattering. An inscattering reaction occurs when a neutron belonging to the packet described by a volume element $\mathrm{d}V$ with energies in $\mathrm{d}E'$ about E' and directions within $\mathrm{d}\hat{\boldsymbol{\Omega}}'$ about $\hat{\boldsymbol{\Omega}}'$ undergoes a scattering event leaving the neutron traveling in $\mathrm{d}\hat{\boldsymbol{\Omega}}$ about $\hat{\boldsymbol{\Omega}}$ with energy in $\mathrm{d}E$ about E, adding this neutron to the packet $(\boldsymbol{r},\hat{\boldsymbol{\Omega}},E,t)$. The probability of neutrons with energy E' and direction $\hat{\boldsymbol{\Omega}}'$ which scatter into the energy $E+\mathrm{d}E$ with direction in $\hat{\boldsymbol{\Omega}}+\mathrm{d}\hat{\boldsymbol{\Omega}}$ can be written as:

$$\begin{aligned}&\text{Probability of neutrons entering}\\&\text{packet due to inscattering}\end{aligned} \equiv \Sigma_s(\boldsymbol{r},\hat{\boldsymbol{\Omega}}'\rightarrow\hat{\boldsymbol{\Omega}},E'\rightarrow E,t)vN(\boldsymbol{r},\hat{\boldsymbol{\Omega}}',E',t). \tag{3-5}$$

Integrating definition 3-5 over all initial energies $\mathrm{d}E'$ and initial directions $\mathrm{d}\hat{\boldsymbol{\Omega}}'$ yields the number of neutrons that enter the packet due to inscattering,

$$\begin{aligned}&\text{Number of neutrons entering}\\&\text{packet due to inscattering}\end{aligned} \equiv \left[\int_{4\pi}\mathrm{d}\hat{\boldsymbol{\Omega}}\int_0^\infty \mathrm{d}E\Sigma_s(\boldsymbol{r},\hat{\boldsymbol{\Omega}}'\rightarrow\hat{\boldsymbol{\Omega}},E'\rightarrow E,t)vN(\boldsymbol{r},\hat{\boldsymbol{\Omega}}',E',t)\right]\mathrm{d}V\,\mathrm{d}\hat{\boldsymbol{\Omega}}\,\mathrm{d}E\Delta t. \tag{3-6}$$

The neutron density at $\boldsymbol{r}+\hat{\boldsymbol{\Omega}}v\Delta t$ at time $t+\Delta t$ is found by adding 3-3, 3-4, and 3-6 and dividing that sum by $\mathrm{d}V\,\mathrm{d}\hat{\boldsymbol{\Omega}}\,\mathrm{d}E$:

$$\begin{aligned}N(\boldsymbol{r}+\hat{\boldsymbol{\Omega}}v\Delta t,\hat{\boldsymbol{\Omega}},E,t+\Delta t) =&\\ N(\boldsymbol{r},\hat{\boldsymbol{\Omega}},E,t)(1-&\Sigma_t v\Delta t)\\ +\left[\int_{4\pi}\mathrm{d}\hat{\boldsymbol{\Omega}}'\int_0^\infty \mathrm{d}E'\Sigma_s(\boldsymbol{r},\hat{\boldsymbol{\Omega}}'\rightarrow\hat{\boldsymbol{\Omega}},E'\rightarrow E,t)N(\boldsymbol{r},\hat{\boldsymbol{\Omega}}',E',t)\right]&\Delta t + S\Delta t.\end{aligned} \tag{3-7}$$

Dividing Eqn. 3-7 and taking the limit as $\Delta t \rightarrow 0$ yields the result, after rearranging terms,

$$\lim_{\Delta t \rightarrow 0}\left[\frac{N(\boldsymbol{r}+\hat{\boldsymbol{\Omega}}v\Delta t,\hat{\boldsymbol{\Omega}},E,t+\Delta t)-N(\boldsymbol{r},\hat{\boldsymbol{\Omega}},E,t)}{\Delta t}\right]+\Sigma_t vN(\boldsymbol{r},\hat{\boldsymbol{\Omega}},E,t) \tag{3-8}$$
$$=\int_{4\pi}\mathrm{d}\hat{\boldsymbol{\Omega}}'\int_0^\infty \mathrm{d}E'\Sigma_s(\boldsymbol{r},\hat{\boldsymbol{\Omega}}'\rightarrow\hat{\boldsymbol{\Omega}},E'\rightarrow E,t)N(\boldsymbol{r},\hat{\boldsymbol{\Omega}}',E',t)+S.$$

Simplifying the first term requires adding and subtracting $N(\boldsymbol{r},\hat{\boldsymbol{\Omega}},E,t+\Delta t)$ to the second term in the numerator of the fraction in Eqn. 3-8 and simplifying the expressions individually. Adding $N(\boldsymbol{r},\hat{\boldsymbol{\Omega}},E,t+\Delta t)$ to the second term in the numerator gives

$$\lim_{\Delta t \rightarrow 0}\left[\frac{N(\boldsymbol{r},\hat{\boldsymbol{\Omega}},E,t+\Delta t)-N(\boldsymbol{r},\hat{\boldsymbol{\Omega}},E,t)}{\Delta t}\right]=\frac{\partial N}{\partial t}. \tag{3-9}$$

Subtracting $N(\boldsymbol{r},\hat{\boldsymbol{\Omega}},E,t+\Delta t)$ from the first term in the numerator leads to a less trivial expression, but it is more readily derived when decomposed in Cartesian coordinates as

$$\lim_{\Delta t \rightarrow 0}\frac{N(\boldsymbol{r}+\hat{\boldsymbol{\Omega}}v\Delta t,\hat{\boldsymbol{\Omega}},E,t)-N(\boldsymbol{r},\hat{\boldsymbol{\Omega}}E,t+\Delta t)}{\Delta t}=$$
$$\lim_{\Delta t \rightarrow 0}\frac{N(x+\Omega_x v\Delta t,y+\Omega_y v\Delta t,z+\Omega_z v\Delta t,\hat{\boldsymbol{\Omega}},E,t))-N(x,y,z,\hat{\boldsymbol{\Omega}},E,t)}{\Delta t}, \tag{3-10}$$

where $\boldsymbol{r}$ and $\hat{\boldsymbol{\Omega}}$ have components $x,\ y,\ z$ and $\Omega_x,\ \Omega_y,\ \Omega_z$ respectively. The infinitesmal $\hat{\boldsymbol{\Omega}}v\Delta t$ is equivalent to Δx. Equation 3-10 is then solved using the chain rule.

$$\lim_{\Delta t \rightarrow 0}\frac{N(x+\Delta x,y+\Delta y,z+\Delta z)-N(x,y,z)}{\Delta t}=$$
$$\frac{\Delta N}{\Delta x}\frac{\Delta x}{\Delta t}+\frac{\Delta N}{\Delta y}\frac{\Delta y}{\Delta t}+\frac{\Delta N}{\Delta z}\frac{\Delta z}{\Delta t}=$$
$$v\Omega_x\frac{\partial N}{\partial x}+v\Omega_y\frac{\partial N}{\partial y}+v\Omega_z\frac{\partial N}{\partial z}=v\hat{\boldsymbol{\Omega}}\cdot\boldsymbol{\nabla}N \tag{3-11}$$

Inserting the results of Eqn. 3-9 and Eqn. 3-11 into Eqn. 3-8, and using the definition

$$\varphi(\boldsymbol{r},\hat{\boldsymbol{\Omega}},E,t)\equiv N(\boldsymbol{r},\hat{\boldsymbol{\Omega}},E,t)v \tag{3-12}$$

yields the NTE,

$$\frac{1}{v}\frac{\partial\varphi}{\partial t} + \hat{\boldsymbol{\Omega}}\cdot\boldsymbol{\nabla}\varphi + \Sigma_t\varphi(\boldsymbol{r},\hat{\boldsymbol{\Omega}},E,t) = \int_{4\pi}\mathrm{d}\hat{\boldsymbol{\Omega}}'\int_0^\infty \mathrm{d}E'\Sigma_s(\boldsymbol{r},\hat{\boldsymbol{\Omega}}',E',t)\varphi(\boldsymbol{r},\hat{\boldsymbol{\Omega}}',E',t) + S(\boldsymbol{r},\hat{\boldsymbol{\Omega}},E,t). \tag{3-13}$$

3.1.1 External Neutron Sources

Discussion of external sources is precluded in the previous section since external source can be handled has boundary conditions when solving for the neutron flux. However, it is important to take a moment to discuss internal source as many texts simply introduce internal source, but provide little further discussion.

A brief dimensional analysis can provide insight into how source terms are defined in the NTE. Since the neutron transport equation describes the number of neutrons in a volume at a point in time, then the units must be $\frac{neutrons}{Length^3 Time}$, or in SI units $\frac{neutrons}{cm^3 s}$. This is easily confirmed by checking the units of one term in Eqn. 3-13. Analyzing the dimensions of the interaction term,

$$\Sigma_t\varphi(\boldsymbol{r},\hat{\boldsymbol{\Omega}},E,t) \equiv \left[\frac{1}{Length}\right]\left[\frac{neutrons}{Length^2 Time}\right] = \left[\frac{neutrons}{Length^3 Time}\right], \tag{3-14}$$

which confirms the previous statement. Therefore, any source term must have these same units.

Neutron sources can be categorized into two types: 1) flux-driven sources and 2) decay reactions. The distinction is made by how the source strength, or the number of neutrons per volume per unit time, varies with the radiation flux. In flux-driven sources, the source strength changes proportionally with the radiation flux. That is because these sources produce neutrons through reactions that occur when radiation interacts with the target nucleus and produces neutrons. Decay reaction sources do not depend on the neutron flux. Instead, these decay reactions, or simply decays, occur when a nucleus is left in an unstable energy state, typically resulting from some other nuclear reaction. These nuclei need to release energy in order to arrive at a stable energy state. Occasionally,

nuclei get rid of excess energy by ejecting one or more neutrons. Flux-driven sources are handled as boundary conditions when solving the mathematical models. Decay reaction sources show up as the source term, S, in the diffusion approximation.

3.2 Reduction of NTE

Upon inspection of Eqn. 3-13, there are four derivatives on the left-hand side of the equation (one in time and three spatial derivatives) and three integrals on the right-hand side of the equation (one in energy and two in direction). Equations containing both integrals and derivatives are called integro-differential equation and are among the hardest forms of problems to solve. Further, the NTE is a function of seven variables; three spatial, two direction, one energy, and one time. In its current form, the NTE has no complete analytic solution. Therefore, assumptions and approximations are applied to reduce Eqn. 3-13 into a tractable form. The following sections will discuss how the multigroup discrete ordinates equation and the 1-D planar diffusion approximation are derived from the NTE.

3.2.1 Treatment of Time Dependence

The time dependence is contained in the first term in Eqn. 3-13. Assuming the neutron flux is unchanging or slowly changing in time will simplify the time-derivative to zero. This is a fair assumption since the time between neutron interactions is much smaller than the time over which the neutron flux is evolving [37]. In this assumption φ is taken to be independent of time, and

$$\frac{\partial \varphi}{\partial t} = 0. \tag{3-15}$$

Then Eqn. 3-13 becomes the steady-state neutron transport equation,

$$\hat{\boldsymbol{\Omega}} \cdot \boldsymbol{\nabla} \varphi(\boldsymbol{r}, \hat{\boldsymbol{\Omega}}, E) + \Sigma_t(\boldsymbol{r}, E)\varphi(\boldsymbol{r}, \hat{\boldsymbol{\Omega}}, E) = \int_{4\pi} \mathrm{d}\hat{\boldsymbol{\Omega}}' \int_0^\infty \mathrm{d}E' \Sigma_s(E' \to E, \hat{\boldsymbol{\Omega}}' \to \hat{\boldsymbol{\Omega}}) \varphi'(\boldsymbol{r}, \hat{\boldsymbol{\Omega}}', E')) + s(\boldsymbol{r}, E, \hat{\boldsymbol{\Omega}}). \tag{3-16}$$

Even after eliminating the partial derivative in time, Eqn. 3-13 is still not tractable due to the three spatial derivatives and three integrals. Therefore, further reduction is necessary.

3.2.2 Reduction to 1-D Planar

Reducing the problem from three spatial dimensions to one spatial dimension eliminates two of the three spatial derivatives and one of the two direction derivatives. As an aside, the components of the direction vector $\hat{\mathbf{\Omega}}$ are ϕ and θ components. ϕ is the azimuthal angle and θ is the polar angle. It is common to define the variable μ in terms of θ as

$$\mu \equiv \cos\theta,$$

where μ is defined over the range [-1, 1] and ϕ is defined over the range [0, 2π]. Integrating Eqn. 3-16 over y, z, and ϕ reduces the dimensionality of the problem as

$$\int_{-\infty}^{\infty} \mathrm{d}y \int_{-\infty}^{\infty} \mathrm{d}z \int_{0}^{2\pi} \mathrm{d}\phi \hat{\mathbf{\Omega}} \cdot \boldsymbol{\nabla} \varphi(\boldsymbol{r}, \hat{\mathbf{\Omega}}, E) + \Sigma_t(\boldsymbol{r}, E)\varphi(\boldsymbol{r}, \hat{\mathbf{\Omega}}, E) - \int_{4\pi} \mathrm{d}\hat{\mathbf{\Omega}}' \int_{0}^{\infty} \mathrm{d}E' \Sigma_s(E' \to E, \hat{\mathbf{\Omega}}' \to \hat{\mathbf{\Omega}}) \varphi'(\boldsymbol{r}, \hat{\mathbf{\Omega}}', E')) + s(\boldsymbol{r}, E, \hat{\mathbf{\Omega}}).$$

Solving the integrals yields:

$$\mu \frac{\partial}{\partial x} \varphi(x, E, \mu) + \Sigma_t(x, E)\varphi(x, E, \mu) = 2\pi \int_{0}^{\infty} \int_{-1}^{1} \Sigma_s(x, E', \mu' \to E, \mu) \varphi(x, E', \mu') \, \mathrm{d}\mu' \, \mathrm{d}E' + S(x, E, \mu). \tag{3-17}$$

Eqn. 3-17 is the steady-state 1-D planar form of the NTE. While this equation appears much simpler to solve, the derivative on the left-hand side and two integrals on the right-hand side indicate the equation is still an integro-differential equation and further simplification is required to arrive at a tractable form. There are two common reductions to Eqn. 3-17, 1) the multigroup discrete ordinates approximation and 2) the diffusion approximation. The following sections apply each of these approximations to

the NTE in order to arrive at two tractable forms of the NTE which will be used in the remainder of this work.

3.3 Multigroup Discrete Ordinates Approximation

The multigroup discrete ordinates equations handle the two integrals on the right-hand side of Eqn. 3-17 by treating the integral over energy as integrals over energy ranges and approximating the integral over μ by evaluating the neutron flux at discrete angles within the full range of [-1, 1]. The final result is a set of coupled, first-order ordinary differential equations that are analytically tractable.

3.3.1 Treatment of Energy Dependence

The first step in developing multigroup equations is to divide the neutron energy range of interest into a finite number of energy groups, E_g, where $g = 1, 2, ..., G$. The order of the energy group number is such that energy decreases as the group number increases, (e.g., $E_g > E_{g+1}$) [36]. Energy groups are typically chosen such that the cross section shows little variation within a group. This is done in order for the group averaged cross section to best represent the energy-dependent cross section values of that group.

The 1-D planar time-independent neutron transport equation, Eqn. 3-17, is reproduced below for the readers convenience.

$$\mu\frac{\partial}{\partial x}\varphi(x,E,\mu)+\Sigma_t(x,E)\varphi(x,E,\mu) = 2\pi\int_0^\infty\int_{-1}^1\Sigma_s(x;E',\mu'\to E,\mu)\varphi(x,E',\mu')\,\mathrm{d}\mu'\,\mathrm{d}E' + S(x,E,\mu). \tag{3-17}$$

Integrating Eqn. 3-17 over g yields

$$\underbrace{\int_g \mu\frac{\partial}{\partial x}\varphi(x,E,\mu)\,\mathrm{d}E}_{(1)} + \underbrace{\int_g \Sigma_t(x,E)\varphi(x,E,\mu)\,\mathrm{d}E}_{(2)} = \underbrace{\int_g 2\pi\int_0^\infty\int_{-1}^1\Sigma_s(x;E',\mu'\to E,\mu)\varphi(x,E',\mu')\,\mathrm{d}\mu'\,\mathrm{d}E'\,\mathrm{d}E}_{(3)} + \underbrace{\int_g S(x,E,\mu)\,\mathrm{d}E}_{(4)}, \tag{3-18}$$

where each term will be discussed individually. Before continuing, it is important to define the the group flux and group cross sections as:

$$\varphi_g(x,\mu) \equiv \int_{E_g}^{E_{g-1}} \varphi(x,E,\mu)\,\mathrm{d}E = \int_g \varphi(x,E,\mu)\,\mathrm{d}E, \tag{3-19}$$

$$\Sigma_{t,g}(x,\mu) \equiv \frac{\int_g \Sigma_t(x,E,\mu)\varphi(x,E,\mu)\,\mathrm{d}E}{\varphi_g(x,E,\mu)}, \tag{3-20}$$

$$\Sigma_{s,g'\to g}(x,\mu) \equiv \frac{\int_{g'}\varphi(x,E',\mu)\int_g\int_{-1}^{1}\Sigma_s(x;E',\mu'\to E,\mu)\,\mathrm{d}\mu'\,\mathrm{d}E\,\mathrm{d}E'}{\varphi_{g'}(x,E',\mu)}. \tag{3-21}$$

905 $\varphi_g(x,\mu)$ is the group averaged flux, $\Sigma_{t,g}(x,\mu)$ is the group averaged cross section, and
906 $\Sigma_{s,g'\to g}(x,\mu)$ is the group to group, or transfer, cross section.

907 Definitions 3-19 - 3-21 are used to rewrite Eqn. 3-18 term by term. The first term of
908 Eqn. 3-18 is rewritten in terms of the group flux, 3-19 as

$$\int_g \mu\frac{\partial}{\partial x}\varphi(x,E,\mu)\,\mathrm{d}E = \mu\frac{\partial}{\partial x}\varphi_g(x,\mu). \tag{3-22}$$

Rewriting the second term in Eqn. 3-18 using the total group cross section, Eqn. 3-20, yields

$$\int_g \Sigma_t(x,E,\mu)\varphi(x,E,\mu)\,\mathrm{d}E = \Sigma_{t,g}(x,\mu)\varphi_g(x,\mu). \tag{3-23}$$

The third term in Eqn. 3-18 requires a bit more work. If the integral of $\mathrm{d}E'$ is taken over each individual energy group rather than over 0 to ∞, then

$$\int_0^\infty \mathrm{d}E' = \sum_{g'=1}^{G}\int_{E_{g'}}^{E_{g'-1}}\mathrm{d}E' = \sum_{g'=1}^{G}\int_{g'}\mathrm{d}E',$$

and the third term can be expressed using group constants, Eqn. 3-24.

$$\int_{g'}\varphi(xE',\mu)\int_g\Sigma(x;E',\mu'\to E,\mu)\,\mathrm{d}E\,\mathrm{d}E' = \sum_{g'=1}^{G}\Sigma_{g'\to g}(x,\mu)\varphi_{g'}(x,\mu) \tag{3-24}$$

Finally, the fourth term is the group source term, Eqn. 3-25. The group source term describes an arbitrary internal source of neutrons with energy in group g.

$$\int_g S(x, E, \mu)\, \mathrm{d}E \equiv S_g(x, \mu). \tag{3-25}$$

Using the redefined terms, Eqns. 3-22 - 3-25, Eqn. 3-18 becomes a set of equations characterizing the flux in each energy group:

$$\mu \frac{\partial \varphi_g}{\partial x} + \Sigma_{t,g}\varphi_g = 2\pi \sum_{g'=1}^{G} \int_{-1}^{1} \Sigma_{s,g'\to g}\varphi_{g'} + S_g, \qquad g = 1, 2, ..., G. \tag{3-26}$$

3.3.2 Treatment of Directional Dependence

Equation 3-26 is a set of monoenergetic neutron transport equations where each equation defines the flux for the energy group g.Therefore, if a method for handling the directional dependence can be found for a single equation in the set of equations, the same method can be extended to all equations in Eqn. 3-26. The discrete ordinates method can be used to handle the integral over μ. By first assuming isotropic scattering, the in-scattering term reduces to

$$2\pi \sum_{g'=1}^{G} \int_{-1}^{1} \Sigma_{s,g'\to g}\varphi_{g'}\, \mathrm{d}\mu' = \frac{1}{2} \sum_{g'=1}^{G} \Sigma_{s,g'\to g} \int_{-1}^{1} \varphi_{g'}\, \mathrm{d}\mu',$$

and Eqn. 3-26 reduces to

$$\mu \frac{\partial \varphi_g}{\partial x} + \Sigma_{t,g}\varphi_g = \frac{1}{2} \sum_{g'=1}^{G} \Sigma_{s,g'\to g} \int_{-1}^{1} \varphi_{g'} + S_g, \qquad g = 1, 2, ..., G. \tag{3-27}$$

Discrete ordinates treats directional dependence by evaluating the integral over μ at a unique set of directions, $\{\mu_i\}$. Evaluating the integral in Eqn. 3-27 at each value of μ_i leads to a weighted sum of neutron fluxes, Eqn. 3-28.

$$\int_{-1}^{1} \varphi_{g'} = \sum_{j=1}^{N} \omega_j \phi_{g'}(x, \mu_j) \tag{3-28}$$

Evaluating Eqn. 3-27 along the set of direction vectors $\{\mu_i\}$, using Eqn. 3-28, results in the multigroup discrete ordinates equations:

$$\mu_i \frac{\mathrm{d}\phi_i^g}{\mathrm{d}x} + \Sigma_t^g \phi_i^g = \frac{1}{2} \sum_{j=1}^{N} \omega_j \sum_{g'=1}^{G} \Sigma_{s,g' \to g} \phi_j^{g'} + S_i^g, \qquad g = 1, 2, ..., G; i = 1, 2, ..., N. \tag{3-29}$$

For the purpose of this work, a set of equations are derived from Eqn. 3-29 using two energy groups (g= 1,2) and two directions (i= 1, 2). Iterating over both indices one at a time leads to the following set of equations:

$g = 1, i = 1$

$$\mu_1 \frac{\mathrm{d}\phi_1^1}{\mathrm{d}x} + \Sigma_t^1 \phi_1^1 = \frac{1}{2} \left(\Sigma_s^{1\to1} \omega_1 \phi_1^1 + \Sigma_s^{1\to1} \omega_2 \phi_2^1 + \Sigma_s^{2\to1} \omega_1 \phi_1^2 + \Sigma_s^{2\to1} \omega_2 \phi_2^2 \right) + S_1^1; \tag{3-30}$$

$g = 1, i = 2$

$$\mu_2 \frac{\mathrm{d}\phi_2^1}{\mathrm{d}x} + \Sigma_t^1 \phi_2^1 = \frac{1}{2} \left(\Sigma_s^{1\to1} \omega_1 \phi_1^1 + \Sigma_s^{1\to1} \omega_2 \phi_2^1 + \Sigma_s^{2\to1} \omega_1 \phi_1^2 + \Sigma_s^{2\to1} \omega_2 \phi_2^2 \right) + S_2^1; \tag{3-31}$$

$g = 2, i = 1$

$$\mu_1 \frac{\mathrm{d}\phi_1^2}{\mathrm{d}x} + \Sigma_t^2 \phi_1^2 = \frac{1}{2} \left(\Sigma_s^{1\to2} \omega_1 \phi_1^1 + \Sigma_s^{1\to2} \omega_2 \phi_2^1 + \Sigma_s^{2\to2} \omega_1 \phi_1^2 + \Sigma_s^{2\to2} \omega_2 \phi_2^2 \right) + S_1^2; \tag{3-32}$$

$g = 2, i = 2$

$$\mu_2 \frac{\mathrm{d}\phi_2^2}{\mathrm{d}x} + \Sigma_t^2 \phi_2^2 = \frac{1}{2} \left(\Sigma_s^{1\to2} \omega_1 \phi_1^1 + \Sigma_s^{1\to2} \omega_2 \phi_2^1 + \Sigma_s^{2\to2} \omega_1 \phi_1^2 + \Sigma_s^{2\to2} \omega_2 \phi_2^2 \right) + S_2^2. \tag{3-33}$$

In a material where scattering from lower energy groups to higher energy groups does not occur and there is no internal neutron source, these equations reduce to:

$g = 1, i = 1$

$$\mu_1 \frac{\mathrm{d}\phi_1^1}{\mathrm{d}x} + \Sigma_t^1 \phi_1^1 = \frac{1}{2}\left(\Sigma_s^{1\to 1}\omega_1\phi_1^1 + \Sigma_s^{1\to 1}\omega_2\phi_2^1\right); \tag{3-34}$$

$g = 1, i = 2$

$$\mu_2 \frac{\mathrm{d}\phi_2^1}{\mathrm{d}x} + \Sigma_t^1 \phi_2^1 = \frac{1}{2}\left(\Sigma_s^{1\to 1}\omega_1\phi_1^1 + \Sigma_s^{1\to 1}\omega_2\phi_2^1\right); \tag{3-35}$$

$g = 2, i = 1$

$$\mu_1 \frac{\mathrm{d}\phi_1^2}{\mathrm{d}x} + \Sigma_t^2 \phi_1^2 = \frac{1}{2}\left(\Sigma_s^{1\to 2}\omega_1\phi_1^1 + \Sigma_s^{1\to 2}\omega_2\phi_2^1 + \Sigma_s^{2\to 2}\omega_1\phi_1^2 + \Sigma_s^{2\to 2}\omega_2\phi_2^2\right); \tag{3-36}$$

$g = 2, i = 2$

$$\mu_2 \frac{\mathrm{d}\phi_2^2}{\mathrm{d}x} + \Sigma_t^2 \phi_2^2 = \frac{1}{2}\left(\Sigma_s^{1\to 2}\omega_1\phi_1^1 + \Sigma_s^{1\to 2}\omega_2\phi_2^1 + \Sigma_s^{2\to 2}\omega_1\phi_1^2 + \Sigma_s^{2\to 2}\omega_2\phi_2^2\right). \tag{3-37}$$

3.4 Reduction to Diffusion Approximation

The diffusion approximation is an alternative reduction of the NTE. There are several methods for deriving the diffusion approximation, however, this derivation uses Legendre polynomial expansions to account for angular dependence in the equation. The neutron transport equation can be simplified through the use of spherical harmonics, which in 1-D, reduce to Legendre polynomials to expand the angular flux and source terms while assuming an isotrpic angular differential cross sectio. The 1-D planar, monoenergetic, NTE with isotropic scattering is

$$\mu \frac{\partial}{\partial x}\varphi(x,\mu) + \Sigma_t(x)\varphi(x,\mu) = \frac{1}{2}\int_{-1}^{1} \Sigma_s(x,\mu' \to \mu)\varphi(x,\mu')\,\mathrm{d}\mu' + S(x,\mu) \tag{3-38}$$

Expanding the angular flux with Legendre polynomials separates the directional and spatial components of the angular flux. Legendre polynomials exhibit an orthogonality property, Eqn. 3-39, and a "3-term recursion" relationship, Eqn. 3-40, which are used in

deriving the diffusion approximation.

$$\int_{-1}^{1} d\mu P_l(\mu) P_m(\mu) = \frac{2}{2l+1}\delta_{lm} \tag{3-39}$$

$$(2l+1)\mu P_l(\mu) = (l+1)P_{l+1}(\mu) + (l)P_{l-1}(\mu) \tag{3-40}$$

Expanding the angular flux in Eqn. 3-38 yields:

$$\mu\frac{\partial}{\partial x}\left[\sum_{l}^{\infty}\frac{2l+1}{2}\phi_l(x)P_l(\mu)\right] + \Sigma_t\sum_{l}^{\infty}\frac{2l+1}{2}\phi_l(x)P_l(\mu) = \tag{3-41}$$
$$\frac{1}{2}\int_{-1}^{1} d\mu'\Sigma_s(x,\mu_0)\sum_{l}^{\infty}\frac{2l+1}{2}\phi_l(x)P_l(\mu') + S(x,\mu).$$

Requiring the projections of Eqn. 3-41 against Legendre polynomials of degree m (e.q., P_m) to be equal to 0 leads to

$$\int_{-1}^{1} d\mu\mu\frac{\partial}{\partial x}\left[\sum_{l=0}^{1}\frac{2l+1}{2}\phi_l(x)P_l(\mu)P_m(\mu)\right] + \int_{-1}^{1} d\mu\Sigma_t\sum_{l=0}^{1}\frac{2l+1}{2}\phi_l(x)P_l(\mu)P_m(\mu) = \tag{3-42}$$
$$\frac{1}{2}\int_{-1}^{1} d\mu P_m(\mu)\int_{-1}^{1} d\mu'\Sigma_s(x,\mu_0)\sum_{l=0}^{1}\frac{2l+1}{2}\phi_l(x)P_l(\mu') + \int_{-1}^{1} d\mu S(x,\mu)P_m(\mu).$$

The summation is truncated at $l = 1$ since the first two terms are all that is necessary for finding the diffusion approximation.

Using the recurrence relationship, Eqn. 3-40, in the first term of Eqn. 3-42 yields

$$\sum_{l=0}^{1}\frac{\partial\phi_l(x)}{\partial x}\left[\int_{-1}^{1} d\mu\frac{l+1}{2}P_{l+1}(\mu)P_m(\mu) + \int_{-1}^{1} d\mu\frac{l}{2}P_{l-1}(\mu)P_m(\mu)\right].$$

Applying the orthogonality gives,

$$\frac{(m-1)+1}{2}\frac{2}{2m+1}\frac{\partial\phi_{m-1}(x)}{\partial x} + \frac{m+1}{2}\frac{2}{2m+1}\frac{\partial\phi_{m+1}(x)}{\partial x},$$

or,

$$\frac{m}{2m+1}\frac{\partial\phi_{m-1}(x)}{\partial x} + \frac{m+1}{2m+1}\frac{\partial\phi_{m+1}(x)}{\partial x}.$$

The second term in Eqn. 3-42 is also solved using the orthogonality property as,

$$\Sigma_t \sum_{l=0}^{1} \frac{2l+1}{2} \phi_l(x) \int_{-1}^{1} d\mu P_l(\mu) P_m(\mu)$$

such that,

$$\Sigma_t \sum_{l=0}^{1} \frac{2l+1}{2} \phi_m(x) \frac{2}{2m+1},$$

or,

$$\Sigma_t \phi_m(x).$$

Solving the third term of Eqn. 3-42 involves calculating the values for $P_{l/m}(\mu)$ for $l, m = 0, 1$, which are $P_0(\mu) = 1$ and $P_1(\mu) = \mu$. Note each integral evaluates to 0 when either l or m is odd. Alternatively, the scattering term evaluates to $2\phi_m$ when l and m are 0.

$$\frac{1}{2}\Sigma_s(x,\mu_0) \sum_{l=0}^{1} \frac{2l+1}{2} \int_{-1}^{1} d\mu' \phi_l(x) P_l(\mu') \int_{-1}^{1} d\mu P_m(\mu) = \begin{cases} 2\phi_0; \ l \ and \ m = 0 \\ 0; \ else. \end{cases}$$

And the final term in Eqn. 3-42 is simply redefined as:

$$S_m \equiv \int_{-1}^{1} d\mu S(x, \hat{\mathbf{\Omega}}) P_m(\mu).$$

For an isotropic source, $S_m = 0$ for $m > 0$.

Combining the terms leads to the final set of P_1 equations, Eqns. 3-43 and 3-44.

$$\frac{\partial \phi_1}{\partial x} + \Sigma_t \phi_0 = \Sigma_s \phi_0 + S_0 \tag{3-43}$$

$$\frac{1}{3}\frac{\partial \phi_0}{\partial x} + \frac{2}{5}\frac{\partial \phi_2}{\partial x} + \Sigma_t \phi_1 = S_1. \tag{3-44}$$

If this set of equations were solved for ϕ_0, the result would be the diffusion approximation. Unfortunately, there are three unknowns (ϕ_0, ϕ_1, and ϕ_2) and two equations. In fact, this set of equations will always have more unknown variables than equations. Therefore, a closure condition is needed to truncate the set of equations by setting $\phi_n = 0$ for $n \geq 2$.

Eqn. 3-44 then becomes

$$\phi_1 = \frac{-1}{3\Sigma_t}\frac{\partial \phi_0}{\partial x} \tag{3-45}$$

which is Fick's Law.

Substituting Fick's Law in Eqn. 3-43 for ϕ_1

$$\frac{\partial}{\partial x}\left[\frac{-1}{3\Sigma_t}\frac{\partial \phi_0}{\partial x}\right] + \Sigma_t \phi_0 = \Sigma_s \phi_0 + S_0,$$

which simplifies to the 1-D, mono-energetic, steady state diffusion approximation:

$$-D\frac{\partial^2 \phi_0}{\partial x^2} + \Sigma_a \phi_0 = S_0, \tag{3-46}$$

where D, the diffusion coeffificent is defined as

$$D \equiv \frac{-1}{3\Sigma_t}, \tag{3-47}$$

when D is independent of x.

3.5 Cylindrical to Polar Coordinate Shift

The cylindrical shape of the spent fuel cask immediately lends to a cylindrical geometry for the mathematical models. However, given the large radius of the cask, it is expected that there exists a point along the radius of the cask where polar geometry can be relaxed to a planar geometry with negligible effect to the neutron flux. This point can be found through a dimensional analysis by developing non-dimensional forms for both the radial and planar diffusion equations.

Non-dimensional analysis is a process where an equation is rewritten in a manner such that there are no units in the problem (i.e., all parameters and variables in an expression are redefined using ratios rather than dimensional quantities). A comparison can be made between the non-dimensional forms of the 1-D polar diffusion approximation and 1-D planar diffusion approximation to determine the location where planar geometry is appropriate.

Starting with the geometry-independent diffusion equation, equation **??**, where D is the diffusion coefficient, ϕ is the scalar flux, Σ_a is macroscopic absorption cross section, and S is the source term. The monoenergetic, steady-state, 1-D planar diffusion approximation:

$$-D\frac{\mathrm{d}^2\phi}{\mathrm{d}x^2} + \Sigma_a\phi = S. \tag{3-46}$$

Diving the equation by $-D$ and defining $L^{-2} \equiv \frac{\Sigma_a}{D}$,

$$\frac{\mathrm{d}^2\phi}{\mathrm{d}x^2} - \frac{1}{L^2}\phi + \frac{S}{D} = 0. \tag{3-48}$$

Non-dimensionalizing x,

$$\tilde{x} = \frac{x}{L}, \tag{3-49}$$

where $\tilde{x}$ is the non-dimensionalized form of x. The first derivative becomes

$$\mathrm{d}x = L\,\mathrm{d}\tilde{x} \tag{3-50}$$

in non-dimensional form.

The second order differential of x, $\mathrm{d}x^2$, becomes

$$\mathrm{d}x^2 = L^2 d\,\mathrm{d}\tilde{x}. \tag{3-51}$$

Eqn. 3-46 then becomes

$$\frac{1}{L^2}\frac{\mathrm{d}^2\phi}{\mathrm{d}x^2} - \frac{1}{L^2}\phi + \frac{S}{D} = 0,$$

or,

$$\frac{\mathrm{d}^2\phi}{\mathrm{d}\tilde{x}^2} - \phi + \frac{L^2S}{D} = 0. \tag{3-52}$$

Note: $\frac{L^2S}{D}$ has units of $Length^{-2}Time^{-1}$, which are the same units as ϕ. So,

$$\tilde{\phi} = \frac{\phi}{L^2S/D}, \tag{3-53}$$

or,

$$\phi = \tilde{\phi}\frac{L^2S}{D}, \tag{3-54}$$

where $\tilde{\phi}$ is the non-dimensionalized form of ϕ. The second differential of ϕ becomes

$$d^2\phi = \frac{L^2 S}{D} d^2\tilde{\phi}. \tag{3-55}$$

Using $\tilde{\phi}$, Eqn. 3-52 is written as

$$\frac{L^2 S}{D}\frac{\mathrm{d}^2\tilde{\phi}}{\mathrm{d}\tilde{x}^2} - \frac{L^2 S}{D}\tilde{\phi} + \frac{L^2 S}{D} = 0, \tag{3-56}$$

or,

$$\frac{\mathrm{d}^2\tilde{\phi}}{\mathrm{d}\tilde{x}^2} - \tilde{\phi} + 1 = 0. \tag{3-57}$$

The 1-D planar diffusion approximation is now expressed in a non-dimensional form.

Expressing the gradient in Eqn. 3-46 in 1-D polar coordinates yields

$$\frac{1}{r}\frac{\mathrm{d}}{\mathrm{d}r}\left(r\frac{\mathrm{d}\phi}{\mathrm{d}r}\right) - \frac{1}{L^2}\phi + \frac{S}{D} = 0, \tag{3-58}$$

or,

$$\frac{\mathrm{d}^2\phi}{\mathrm{d}r^2} + \frac{1}{r}\frac{\mathrm{d}\phi}{\mathrm{d}r} - \frac{1}{L^2}\phi + \frac{S}{D} = 0. \tag{3-59}$$

Let

$$\tilde{r} = \frac{r}{L}, \tag{3-60}$$

and,

$$\tilde{\phi} = \frac{\phi D}{L^2 S} \tag{3-61}$$

Using the non-dimensionalized variables defined in Eqns. 3-60 and 3-61, Eqn. 3-59can be rewritten as

$$\frac{\mathrm{d}^2\tilde{\phi}}{\mathrm{d}\tilde{r}^2} + \frac{1}{\tilde{r}}\frac{\mathrm{d}\tilde{\phi}}{\mathrm{d}\tilde{r}} - \tilde{\phi} + 1 = 0. \tag{3-62}$$

Then, the curvilinear form of the diffusion equation is

$$\frac{\mathrm{d}^2\tilde{\phi}}{\mathrm{d}\tilde{r}^2} + \frac{k}{\tilde{r}}\frac{\mathrm{d}\tilde{\phi}}{\mathrm{d}\tilde{r}} - \tilde{\phi} + 1 = 0, \tag{3-63}$$

where $k = 0$ for planar geometries and $k = 1$ for cylindrical geometries. Further, plotting the variable $\frac{k}{\tilde{r}}$ for $k = 1$ will show the location where accounting for polar geometries

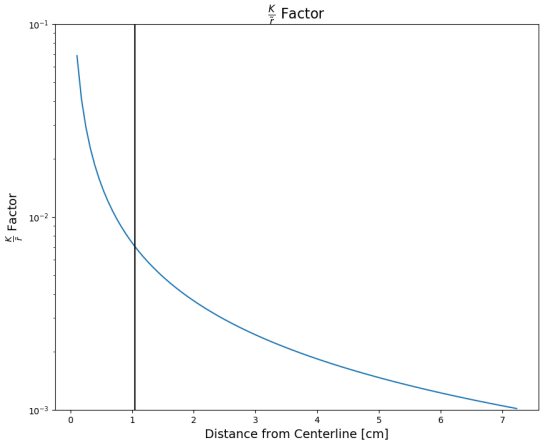

Figure 3-1. As the factor $\frac{k}{\tilde{r}}$ decreases, the planar solutions better approximate polar solutions in the homogenous fuel material. The location of the black vertical line shows the point where the factor $\frac{k}{\tilde{r}}$ is 10% of its initial value.

becomes negligible. Figure 3-1 shows the result from the previous dimensional analysis using material properties of the fuel materials. Near 1cm into the fuel material, results calculated using a cylindrical and planar geometries agree within 10% (denoted by the vertical black line in Fig. 3-1). After 1cm materials can be approximated using planar equations, however, the flux in the fuel region will need to be approximated using a polar diffusion equation.

CHAPTER 4
ANALYSIS OF SUB-PROBLEMS

This chapter analyzing each sub-problem in depth according to the results assessment methodology using the mathematical models identified in Sec. 2 and derived in Sec. 3. Through the explanation of the causes of each feature, confidence is gained in the correctness of the detailed MCNP simulation.

4.1 Discussion of Sub-problems

4.1.1 Flat Region

Initially, the flatness of the first feature suggests that a reduction in fine structure detail can be used to adequately represent a substantial portion the fuel region. Each fuel pin is approximately 1cm in diameter, yet the neutron flux spatial distribution does not show variations at the centimeter level. Fluctuations in the neutron flux spatial distribution at the centimeter level would require any simplified models to also preserve geometric structures at the centimeter level, but the absence of these fluctuations implies that geometric reductions are possible. Therefore, an MCNP model is developed with a homogenized fuel in the MPC similar to the analytic model.

For the purpose of clarity, this fuel composition is called "fully homogenized" since it incorporates all the materials inside the MPC. The fully homogenized fuel composition is determined by calculating the mass fractions of each material in the MPC (the stainless steel basket, the neutron absorbing pads, the helium backfill, and the fuel rods). Finally, the density of the fully homogenized fuel is corrected to account for the various densities of each material in the MPC (10.44 $\frac{g}{cm^3}$ for a single fuel rod vs. 2.31 $\frac{g}{cm^3}$ for the fully homogenized fuel). The entire interior volume of the MPC is filled with the fully homogenized fuel material. Figure 4-1 is a cross section view of the corresponding MCNP model using the fully homogenized fuel material. This model is referred to as the "homogenous model".

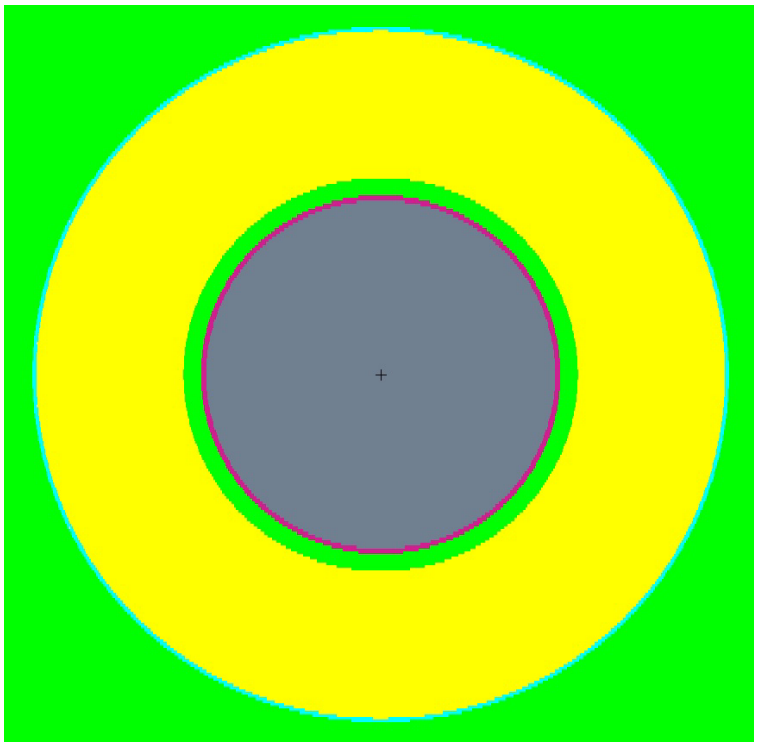

Figure 4-1. The homogeneous model. The gray circle is the fully homogenized fuel which fills the entire volume interior to the MPC.

Figure 4-2 shows the homogeneous model neutron flux spatial distribution through the fuel region of the MPC, together with the complementary result from the detailed model. The homogenous model over predicts the neutron flux spatial distribution by 20-25% through the fuel region. Even though the reduced model overpredicts the detailed flux, the shape of the neutron flux spatial distribution predicted in both models shows a steady decrease across the inner 65 cm. The relative flatness of the two fluxes is evidence that geometric attenuation is less important than the material properties within the MPC. To further corroborate this notion, Fig. 4-2 also includes results from an analytic model: the dotted line appearing in this figure is a result from monoenergetic, 1D cylindrical diffusion theory. In this analytic setting, the monoenergetic scalar neutron flux across a 1D cylindrical region with constant material properties is given by

$$\phi(r) = \frac{\alpha}{DB^2}\left(1 - \frac{I_0(Br)}{I_0(B\tilde{r})}\right); \qquad B \equiv \sqrt{\frac{\Sigma_a - \bar{\nu}\Sigma_f}{D}}. \tag{4-1}$$

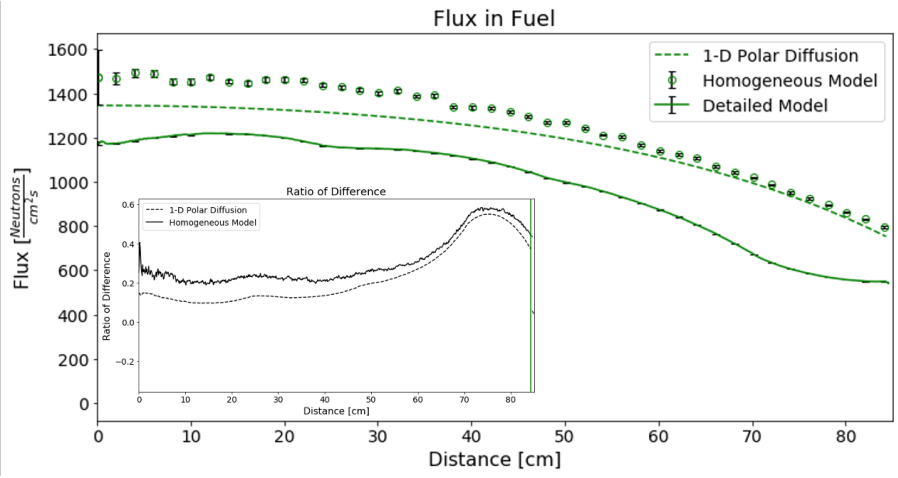

Figure 4-2. The results of the simulated neutron flux spatial distribution from the homogenous model (circles) is similarly flat to the neutron flux spatial distribution of the detailed model (solid line). The flux calculated using the diffusion approximation (dotted line) is also plotted against the two MCNP models. The diffusion approximation also shows the flatness of the neutron flux spatial distribution.

where α is the intrinsic neutron source, B is the material buckling as indicated in terms of the macroscopic total absorption cross section Σ_a, macroscopic fission cross section Σ_f, and mean number of neutrons per fission $\bar{\nu}$, and diffusion coefficient D, I_0 is the modified Bessel function of the first kind, and $\tilde{r}$ is the extrapolated radius of the fuel region. The spatial curvature of the scalar flux appearing in Eq. 4-1 is controlled principally by the material buckling B; as the value of B increases (resulting when absorption physics is dominant over scattering physics) the neutron flux spatial distribution calculated in Eq. 4-1 produces a flat distribution in r - as in fuel region of both computational models. This result is discussed further in conjunction with the sensitivity discussion corresponding to the diffusion approximation. The flatness of the diffusion model is proof that the flatness seen in the MCNP models is due to material properties being dominant over geometry. While the diffusion model captures the essential physics giving rise to the flat flux region, it does not adequately capture the abrupt level off within the fuel region for $r > 65$cm.

4.1.2 Abrupt Level-off Region

In order to better capture the physics which describes the second feature, a second model is developed. The purpose of this model is to capture the physics associated with the neutron flux spatial distribution suddenly flattening before exiting the MPC.

Intuitively, since geometric attenuation is minimal and the mfp for neutrons (70,000 cm at 1 MeV) is much greater than the thickness of the region between the fuel basket and MPC wall (10 cm), a free streaming (i.e., constant flux) approximation is likely to be valid there. To corroborate this notion, the homogeneous model is further modified to add an annulus of helium around a fuel region which is reduced in radius in a manner which preserves the volume of the original 32 fuel cells. This model is referred to as the "helium model". Fig. 4-3 shows the difference between the homogenous and helium models. The composition of the fuel region is changed to account for the helium now present in the annulus. The new homogenized fuel composition, called the partially homogenized fuel composition, is made using the mass fractions of materials in the 32 fuel cells (the stainless steel fuel basket, the neutron absorbing pads, the helium interior to the fuel cells, the fuel rods) and the density of the material is adjusted to account for the reduced amount of helium (2.95 $\frac{g}{cm^3}$).

Figure 4-4 shows the results of the simulated flux in the helium model as compared to the detailed model. The fuel region, comprised of partially homogenized fuel material, has a smaller radius and the analytic solution is held constant for $r > \tilde{r}$. The increased density of the fuel in the helium model increases the total neutron absorption and thus lowers the amplitude of the neutron flux spatial distribution. The flux flattens out over the last 20 cm, which is a result of adding the non-interacting helium annulus. The helium model better demonstrates that the flatness of the two MCNP models and the analytic model match, with the exception of the three depressions present in the detailed models. These results do show neutrons streaming through the helium region exterior to the fuel cells before exiting into the MPC even though the helium model and the analytic model do not capture the small depressions.

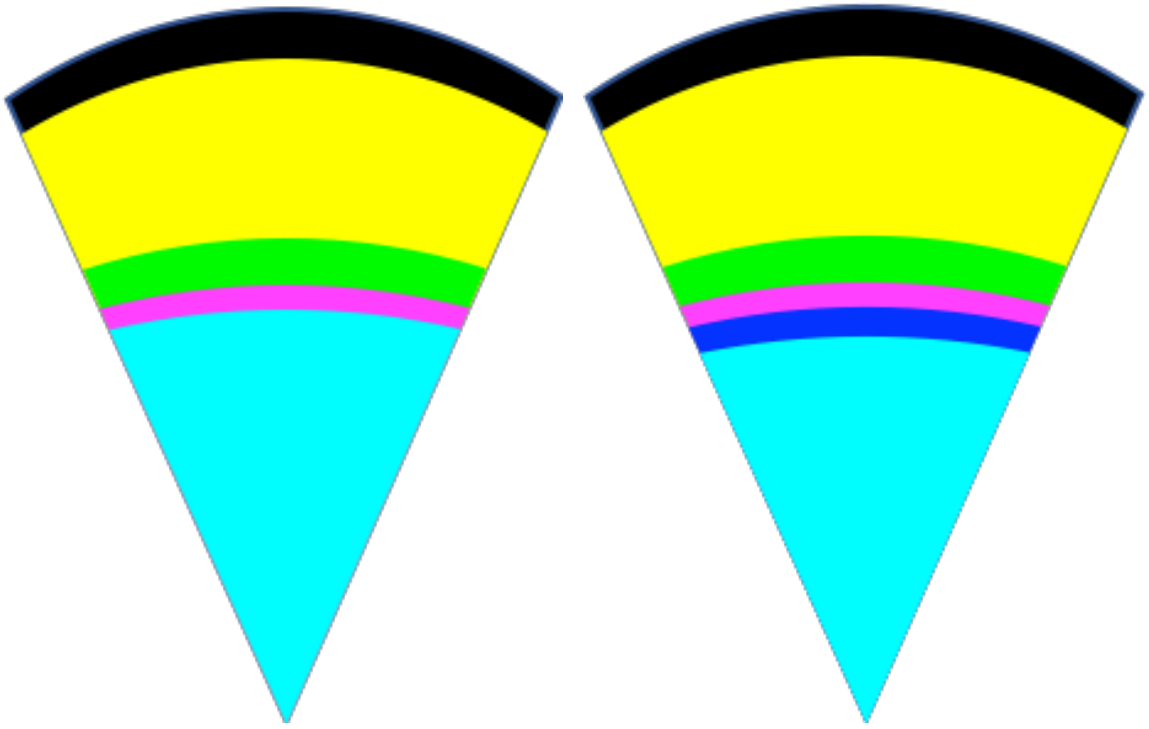

(a) (b)

Figure 4-3. A) Section views of the homogeneous model, B)Helium model. The helium model includes an annulus of helium gas, ∼10 cm thick, added around the homogenized fuel to allow streaming at the edge of the fuel region. Not to scale.

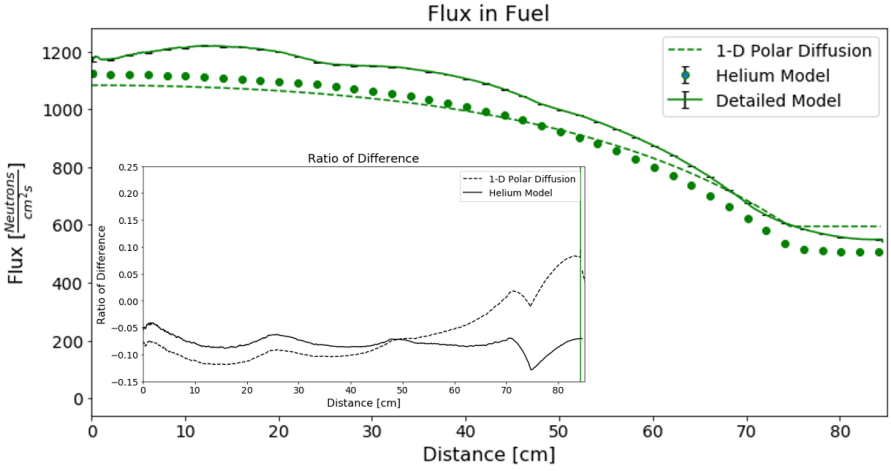

Figure 4-4. The neutron flux spatial distribution simulated by the helium model (circles) captures the neutron flux spatial distribution flattening out in the detailed model (solid line) over the 20 cm region before exiting the fuel region. The diffusion approximation (dotted line) also captures the flux flattening near 65 cm from the cask centerline after adding a helium annulus for neutron streaming.

4.1.3 Inter-bundle Depressions

To this point, the simulation results assessment has shown that explanation of causes for the first two features does not necessitate simulation of geometric details at the individual fuel pin level. However, the physics associated with the three small depressions in the detailed model (seen in Fig. 2-23) has not been explained. Intuition suggests it seems necessary that some level of geometric detail needs to be added back into the reduced complexity simulations to identify the cause of the final two features.

The scalar flux depressions depicted in Fig. 2-23 represent the third feature and are presumed to be caused by the neutron absorbing pads that are present between fuel bundles, located at $-71.62 < x < -71.41$ cm, $-47.61 < x < -47.40$ cm, $-23.61 < x < -23.40$ cm, $0.40 < x < 0.61$ cm, $24.40 < x < 24.61$ cm, $48.41 < x < 48.62$ cm. These pads contain ^{10}B, which has a propensity of absorbing thermal neutrons. To corroborate this notion, reintegrating the stainless steel basket structure and neutron absorbing pads is expected to capture the depressions not found in the previous models. Again, comparing the mfp of neutrons in stainless steel 304, the neutron absorbing pads, and fuel rods in Fig. 4-5 shows the mfp is dominated by the absorbing component at a level of approximately 10cm (or less, depending on the energy of the incident neutrons). These mfp's are similar to the physical thickness of the stainless steel, neutron absorbing pads, and fuel in the MPC. Therefore, the neutrons will undergo an appreciable number of interactions in the stainless steel and neutron absorbing materials. However, unlike in the fuel, no neutrons are being generated in the steel and neutron absorbing materials, and so the flux is expected to decrease therein.

Another MCNP model is developed to describe the cause of the depressions, Fig. 4-6. This multi-layered model is called the "1-D basket model" and represents a single row of fuel cells from the detailed model with one difference: the volume attributed to fuel materials. In this model, the interior volume of each fuel cell contains a cell homogenized fuel composition with helium on both sides and neutron absorbing pad to the left. The cell

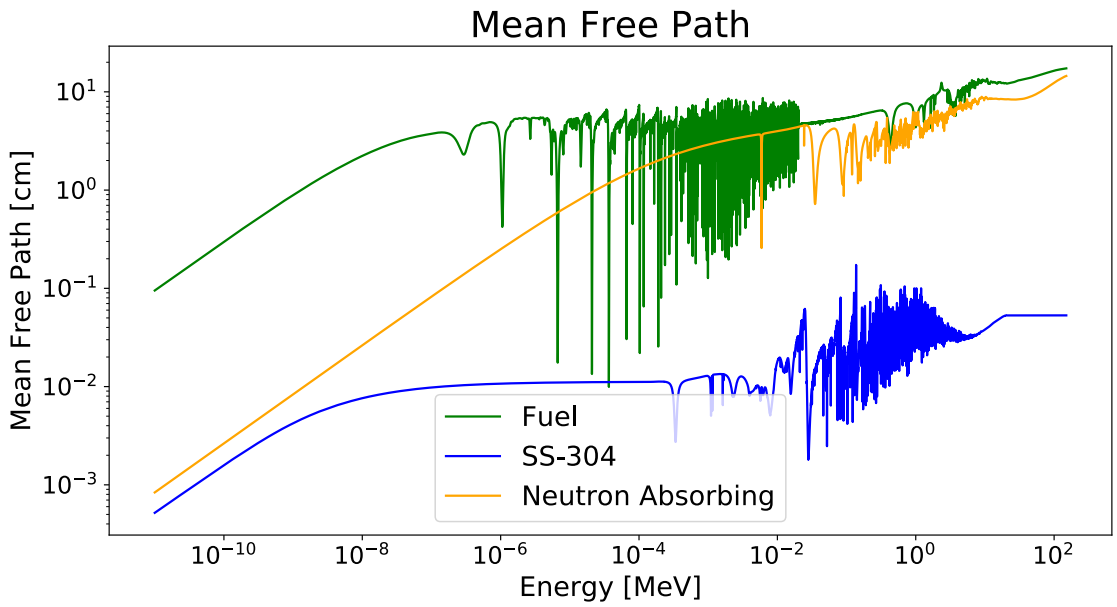

Figure 4-5. The mean free paths for stainless steel 304 (blue), neutron absorbing pad material (orange), and fuel pin material (green). These three mean free paths are similar to the physical thicknesses of each material implying that the steel and neutron absorbing pads need to be included in MCNP simulations as discrete materials instead of being incorporated into the homogenized fuel.

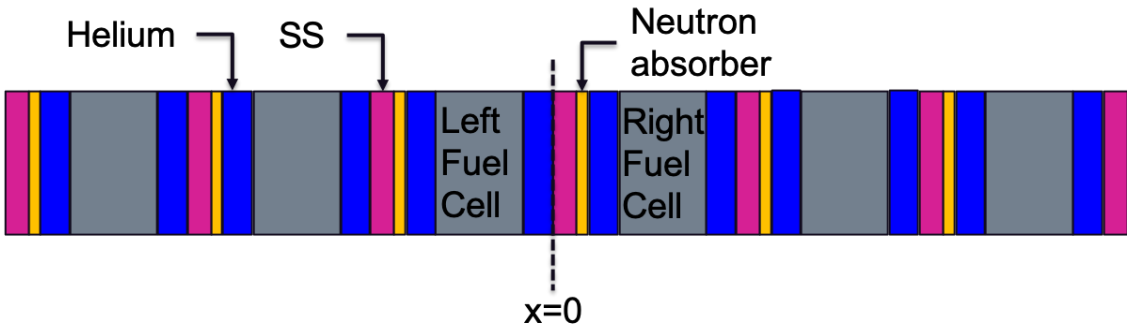

Figure 4-6. The 1-D basket model used to identify the cause of the small depressions. The model is repeating layers of stainless steel (pink), neutron absorbing pads (orange), helium (blue), and cell homogenized fuel (gray).

homogenized fuel composition is determined using the mass fraction of materials which comprise the 264 fuel rods and helium between the fuel rods in each cell. The volume of the cell homogenized fuel material is defined to be equal to the volume of a single fuel bundle.

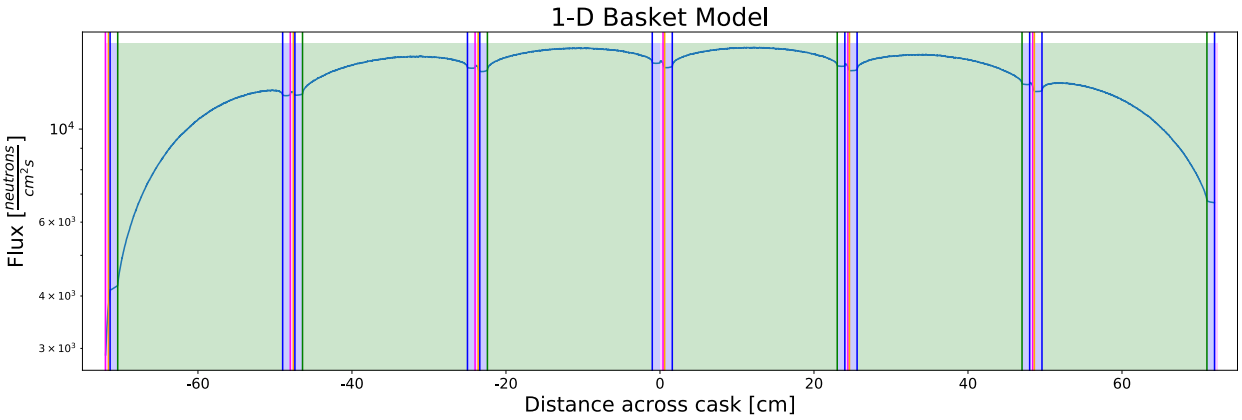

Figure 4-7. The neutron flux spatial distribution simulated from the 1-D basket model. The colors are representative of each material: stainless steel 304 (pink), neutron absorbing pad (orange), helium (blue), and cell homogenized fuel (green). There are depressions present in the flux which occur within the stainless steel and neutron absorbing pads.

The simulated neutron flux spatial distribution through the 1-D basket model is shown in Fig. 4-7. The simplified basket model has six small depressions present in the flux around ±25 cm, ±50 cm, ±75 cm. These depressions correspond to a 1-2 % local reduction in the flux, which is similar in location and magnitude to the depressions present in the simulated neutron flux spatial distribution in the detailed model. The depressions in the neutron flux spatial distribution occur within the stainless steel and neutron absorbing pad materials. The flux increases in the fuel as neutrons are born from spontaneous fission decays and (α, n) reactions. The combination of the absorption events in the neutron absorbing pads and source events in the fuel cause the depressions observed in the neutron flux spatial distribution.

4.1.4 Azimuthally Asymmetric Flux

The final feature, the flux asymmetry (seen in Fig. 2-24), is also explained using the 1-D basket model. The detailed model shows a higher flux leaving the bottom right of section of the cask as compared to the top left section of the cask. This discrepancy is seen at the leftmost and rightmost exiting surfaces in Fig. 4-7. The leftmost face has a lower exiting flux value than the value observed at the rightmost face. Figure 4-6 shows

the reason for the asymmetry: a neutron born in the left fuel cell and traveling left will pass through three neutron absorbing pads before exiting the left face, which is the same number of neutron absorbing pads that same neutron would have to pass through if it were traveling right. Conversely, if a neutron is born in the right fuel cell and traveling to the left, it passes through four neutron absorbing pads. However, if that same neutron were to travel right, it only potentially encounters two neutron absorbing pads. The number of neutron absorbing pads a neutron potentially encounters is not the same based on the the location of neutron generation and direction of travel because of the placement of neutron absorbing pads in the MPC. The asymmetric loading of these pads directly affects the neutron flux spatial distribution exiting the spent fuel cask.

To further corroborate this notion, the detailed model was adjusted, replacing the stainless steel structure and neutron absorbing pads with vacuum. Figure 4-8 compares the ratio of the neutron flux spatial distribution averaged over the top left section and the flux averaged over the bottom right section from the detailed model where one simulation replaced neutron absorbing pads with vacuum and the original detailed model. The maximum deviation of the ratios of neutron flux spatial densities is 0.1% as a result of replacing non-fuel structure in the MPC with vacuum, confirming the results from the basket model. In contrast, the maximum deviation of these same ratios in the original detailed model is nearly 10%.

Previous findings have shown that geometric structures finer than the stainless steel baskets, neutron absorbing pads, and helium annulus are unnecessary for characterization of the spatial flux distribution arising from the detailed model. A final model, the "cruciform model", is developed to ensure no important physics are neglected in the reduced-order modeling and analysis process. This model uses the cell homogenized fuel definition in each of the 32 original fuel cells. In doing so, the stainless steel fuel basket and neutron absorbing pads are retained and discrete from the homogenized fuel. The helium surrounding the 32 fuel cells is also retained.

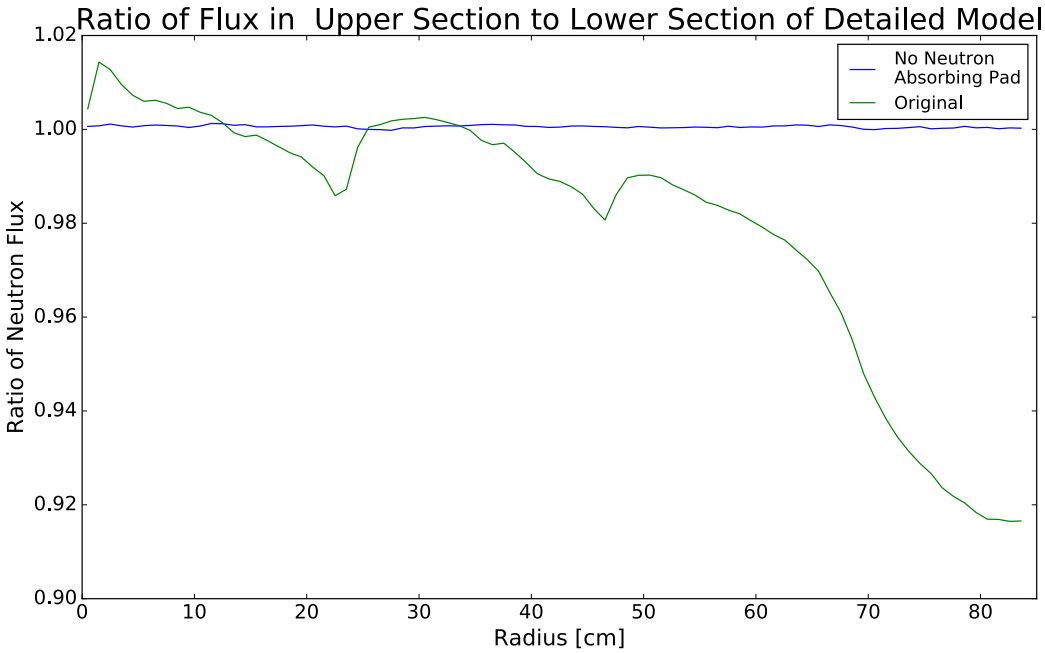

Figure 4-8. The ratio of the neutron flux spatial distribution in the upper left section of the fuel region to the neutron flux spatial distribution in the lower right section of the fuel region. This ratio is nearly 1 over the entirety of the fuel region, confirming the assumption that removing the neutron absorbing pads removes the previously identified depressions.

The neutron spatial flux distribution simulated by the cruciform model is shown in Fig. 4-10. These results underpredicts the flux from the detailed model by 5-7% through the entire fuel region, including in the helium annulus. Moreover, these results can also be interpreted as the cruciform model accounting for the physics relevant to the detailed model's spatial neutron flux distribution at a level greater than 90%. That is, further fine detail additions to the cruciform model will "close the gap" with respect to the detailed model at a sub-10% level.

4.1.5 Non-exponential Decay in Concrete

The hydrogen content in concrete is responsible for thermalizing the neutron flux an attenuating neutrons. Figure 4-11 compares the neutron flux from the detailed model

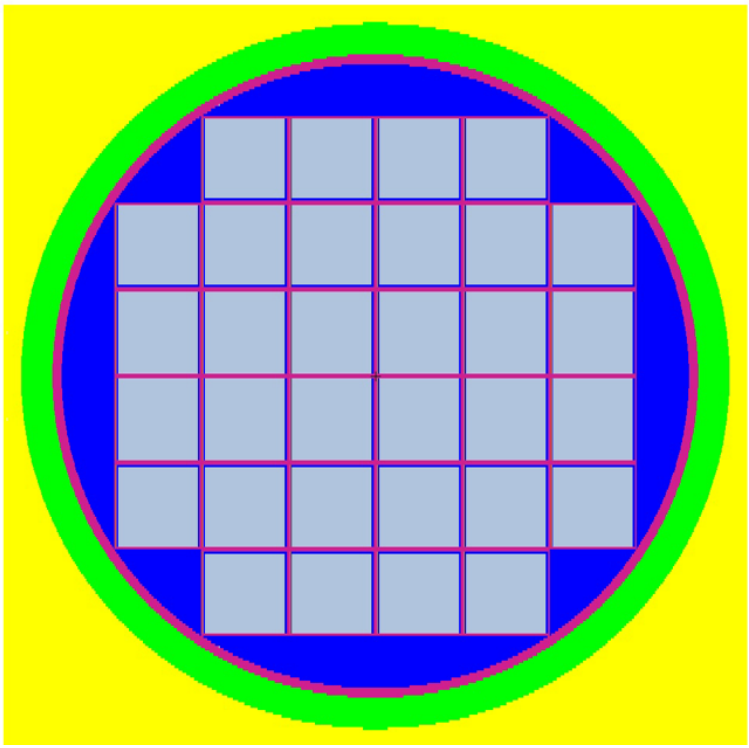

Figure 4-9. The cruciform model. The gray squares are cell homogenized fuel, the stainless steel fuel basket and MPC are pink, the helium annulus is blue, the air exterior to the MPC is green, and concrete is yellow. The neutron absorbing pads (orange) are present in this diagram, but are too thin to be seen here.

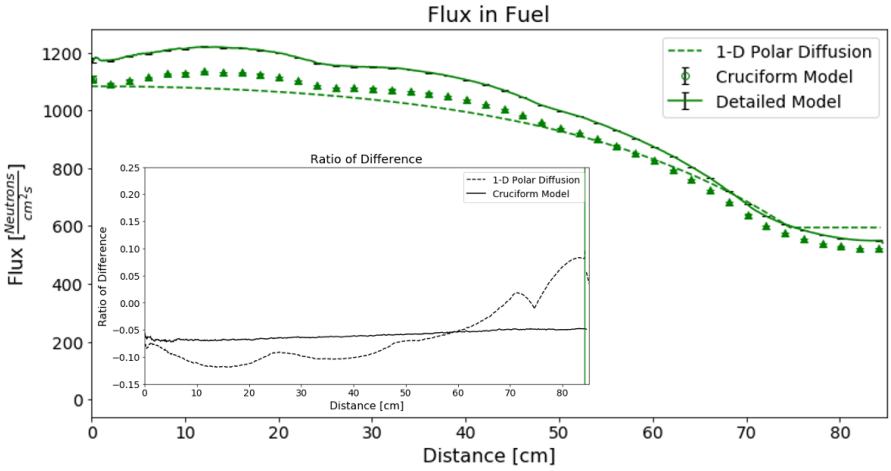

Figure 4-10. The neutron flux spatial distribution of the cruciform model (triangles) capture the flatness of, the leveling off of, and the depressions in the neutron flux spatial distribution seen in the detailed model (solid).

(solid line), the E2S2 analytic solution (red dashed), the fast energy group E2S2 solution (blue dotted), the thermal energy group E2S2 solution (brown dotted), and the MCNP helium model (dotted). In concrete, the neutron flux experiences a shift in energies as a result of downscattering occurring on hydrogen atoms. The analytic solutions confirm the observed shift in energies. The fast flux (the blue dotted line) decreases exponentially through the concrete regions. Intuitively, the exponential decrease is behaves similarly to an uncollided flux calculation, where the uncollided neutron flux decreases exponentially with thickness as neutrons undergo interactions in a material. In the case of concrete these interactions are mainly scattering since the scattering ratio ($\frac{\Sigma_s}{\Sigma_t}$) in the fast region for concrete is 99.5%. A high scattering ratio at fast neutron energies breeds thermal neutrons, a conclusion consistent with the initial increase in the thermal neutron flux in Fig. 4-11. As the fast neutron population decreases, the rate at which neutrons are thermalized decreases as well, which when combined with loss terms, causes the populations of both the fast and thermal neutron fluxes to decrease as a function of thickness. Both the analog MCNP model and the analytic model capture the physics of the detailed model within 10%, with the exception of the last 6cm of the analytic model.

The reason the analytic model shows higher disagreement with the detailed model in the outer 6cm is a result of the boundary conditions. The E2S2 equations are solved using a continuous flux boundary condition at both surfaces of the model. While considering the neutron flux as continuous is a physically consistent boundary condition, higher order effects (e.q., continuity of derivatives) are not being considered. Further, the outermost boundary condition assumptions that no neutrons will re-enter the cask after leaving. While this assumption is nearly physically constituent, it will still act as source of error to materials within the cask.

4.1.6 Flux in MPC and Carbon Steel Shell

The MPC and carbon steel shell are the final material regions left to discuss. The thinness of these materials leads to a relatively simple discussion. Figure 4-12 compares

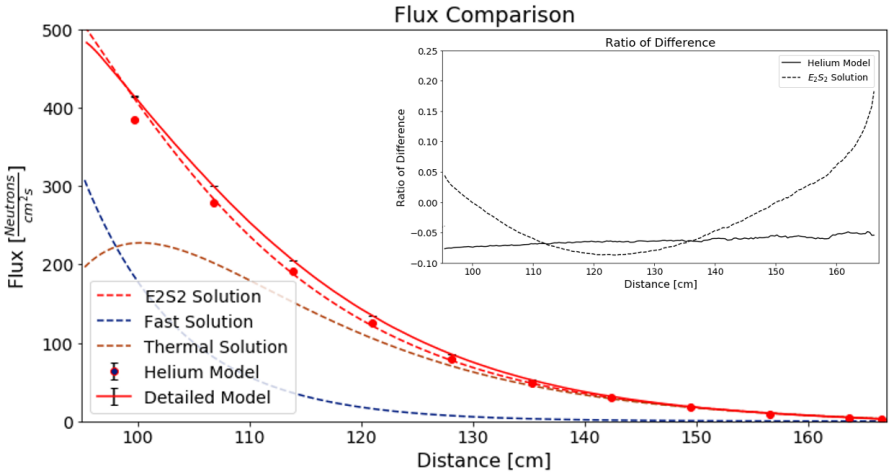

Figure 4-11. The neutron flux spatial distribution of the analytic E2S2 model (dashed line), helium model (circles), and detailed model (solid lines). The fast and thermal portions of the E2S2 solutions are shown in the blue and brown dotted lines respectively. The inset graphs shows the error between the analog models and detailed model.

the neutron flux from the detailed model (solid blue), the E2S2 model solution (dotted blue line), and the analog helium model (circles). The fast and thermal components of the E2S2 solution are displayed as the dark blue and brown lines respectively. Even though the thickness of the stainless steel is a similar to the MFP, some of the fast neutrons undergo scattering interactions and thermalize which results in an increase in the thermal flux. The error between the analog models and the detailed model is less than 10%. In fact, the analytic model agrees with the detailed model within 5%, which is better than the helium model.

Figure 4-13 shows the neutron flux in the carbon steel shell. The flux in the carbon steel shell is almost entirely thermal since the concrete has already thermalized the neutron flux. The analytic model captures this behavior, unfortunately, the analytic model does not capture an increase in source source neutrons in the carbon steel which was observed in the detailed model. This is a result of assuming the number of neutrons bred through interactions is negligible and not including these fast neutrons in the E2S2 model. However, the analytic model agrees within 10-40% over the thickness of the carbon steel.

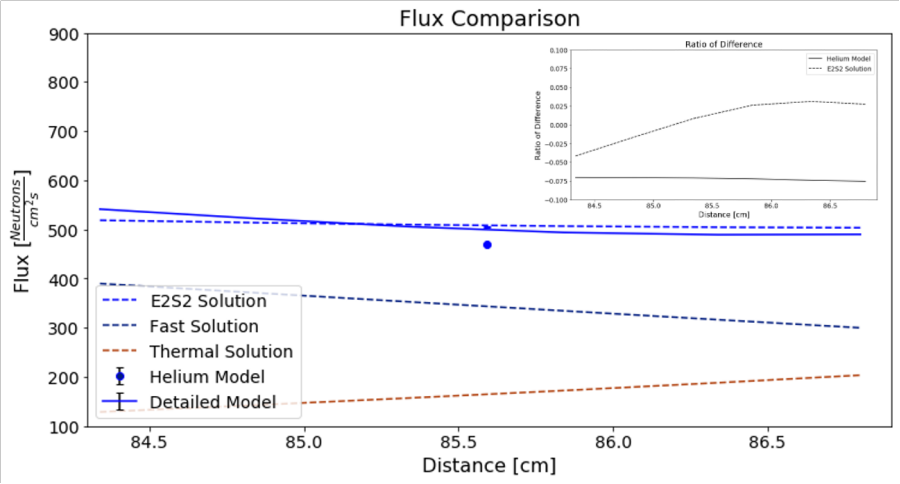

Figure 4-12. The neutron flux spatial distribution of the analytic E2S2 model (dashed line), helium model (circles), and detailed model (solid lines). The fast and thermal portions of the E2S2 solutions are shown in the blue and brown dotted lines respectively. The inset graphs shows the error between the analog models and detailed model.

Overall, this level of agreement is acceptable since the neutron flux is so small, in fact, the flux at the exiting surface of the cask is 0.68 $\frac{1}{cm^2 s}$ as predicted by the detailed model and 0.91 $\frac{1}{cm^2 s}$ as predicted with the E2S2 solution. The scale of the neutron flux is low making the larger error values acceptable. The error between the detailed and analytic models increases through the carbon steel shell as a result of the boundary conditions. At the exiting surface of the cask, the analytic solution is assumed to have a vacuum boundary condition. Meaning, none of the neutrons which leave the cask will return. While this assumption is appropriate (since the cask in the detailed model is surrounded by air), it does not exactly replicate the conditions in the detailed model. The result is an increase in error values near the outer surface of the cask.

4.2 Summary

Using reduced complexity analytic and computational models to analyze the simulation results of a high-fidelity computational model allows for the quantification of effects of any assumptions invoked when developing the latter model. Ensuring important physics are preserved in the course of conducting simulations increases

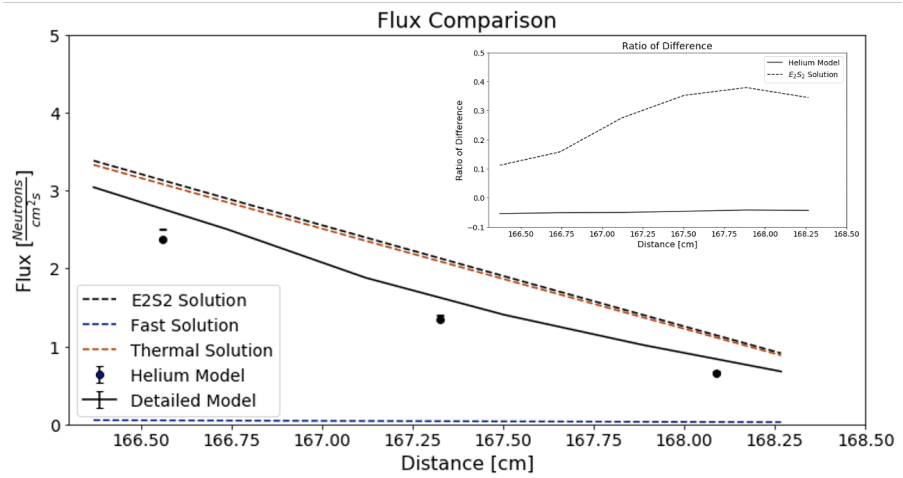

Figure 4-13. The neutron flux spatial distribution of the analytic E2S2 model (dashed line), helium model (circles), and detailed model (solid lines). The fast and thermal portions of the E2S2 solutions are shown in the blue and brown dotted lines respectively. The inset graphs shows the error between the analog models and detailed model.

the likelihood of correct results. This work exemplified this notion through a process referred to as "simulation results assessment." As a demonstration, this work included post-simulation analysis of a detailed MCNP model of a HI STORM 100 spent nuclear fuel cask. A series of reduced analytic and computational models were developed and used to identify the physics which causes features in the neutron flux spatial distribution as calculated by the detailed model. In the HI-STORM 100 model, the stainless steel basket, neutron absorbing pads, and helium annulus around the fuel cells are important physical components that need to be preserved in modeling. Retaining the individual fuel pin structure was found to be less important than broadly capturing the lumped material properties inside the individual fuel cells. These results were corroborated using the cruciform model, which appears to capture the physics relevant to the neutron flux spatial distribution in the detailed model beyond the 90% level. The major features of the neutron flux spatial distribution simulated by the detailed model are expected to be correct since the this model preserves material fuel properties and the geometric structure of the neutron absorbing pads and helium annulus.

REFERENCES

[1] G. Barenblatt, *Flow, Deformation, and Fracture: Lectures on Fluid Mechanics and the Mechanics of Deformable Solids for Mathematicians and Physicists.* Cambridge University Press, 2014.

[2] "Nuclear Power Summary - News & Notes," DOE, Tech. Rep., April 2019.

[3] R. H. J. JR., "Dry cask inventory assessment," Savanah River National Laboratory, Tech. Rep., 2016.

[4] C. Greulich and et. al., "High energy neutrons transmission analysis of dry cask storage," *Nuc. Inst. and Meth. in Phys. Res. A*, vol. 874, pp. 5–11, 2017.

[5] I. Harkness and et al., "Development of neutron energy spectral signatures for passive monitoring of spent nuclear fuels in dry cask storage," *EPJ Web of Conferences-ANIMMA 2017*, vol. 170, 2018.

[6] I. Harkness and et. al., "Feasibility of fast neutron spectroscopy for safegaurds and verification of spent fuel in dry cask storage," Los Alamos National Laboratory, Tech. Rep. LA-UR-18-29519, 2018.

[7] W. Fickett, "Detonation in miniature," *Am. J. Phys.*, vol. 47, no. 12, pp. 1050–1059, 1979.

[8] "Guide for verification and validation in computational solid mechanics," American Society of Mechanical Engineers, American National Standard ASME V&V 10-2006, 2006.

[9] W. L. Oberkampf and T. G. Trucano, "Verification and validation benchmarks," *Nuc. Eng. and Desn.*, no. 238, pp. 716–743, 2008.

[10] P. Knupp and K. Salari, *Verification of Computer Codes in Computational Science and Engineering.* Chapman & Hall/CRC, 2003.

[11] T. Sullivan, *Introduction to Uncertainty Quantification.* Springer, 2015.

[12] D. Cacuci, *Sensitivity and Uncertainty Analysis: Theory.* Chapman & Hall/CRC, 2003, vol. 1.

[13] H. Bode, *Network Analysis and Feedback Amplifier Design.* Van Nostrand-Reinhold, 1945.

[14] M. D. McKay, "Sensitivity analysis," Los Alamos Scientific Laboratory, Tech. Rep. LA-UR-79-982, 1979.

[15] R. Mosteller, "Bibliography of mcnp verification and validation: 2004," Los Alamos National Laboratory, Tech. Rep. LA-UR-04-8965, 2004.

[16] F. B. Brown, "The mcnp6 analytic criticality benchmark suite," Los Alamos National Laboratory, Tech. Rep. LA-UR-16-24255, 2016.

[17] P. Grechanuk and et al., "Semi-analytic benchmarks for mcnp6," *2017 American Nuc. Soc. Annual Meeting*, no. LA-UR-17-20668, 2017.

[18] P. Roache, *Verification and Validation in Computational Science and Engineering*. Hermosa, 1998.

[19] B. C. Kiedrowski and et al., "Mcnp6 shielding validation suite: Past, present, and future," *2011 American Nuc. Soc. Winter Meeting*, 2011.

[20] F. B. Brown, M. E. Rising, and J. L. Alwin, "Verification of mcnp6.2 for nuclear criticality safety applications," Los Alamos National Laboratory, Tech. Rep. LA-UR-17-23822, 2017.

[21] S. Mashnik, "Validation and verification of mcnp6 against intermideat and high-energy experimental data and results by other codes," Los Alamos National Laboratory, Tech. Rep., 2010.

[22] Y. Chen and et. al., "Surface dose rate calculations of a spent-fuel storage cask by using mavric and its comparison with sas4 and mcnp," *Nuclear Thechnology*, vol. 175, no. 1, pp. 343–350, 2017.

[23] A. Chen, Y. Chen, J. Wang, R. Sheu, Y.-W. Liu, and S. Jiang, "A comparison of dose rate calculations for a spent fuel storage cask by using mcnp and sas4," *Annals of Nuclear Engineering*, vol. 35, pp. 2296–2305, 2008.

[24] Thiele.H and F.-M. Borst, "Shielding benchmark calculations with scale/mavric and comparison with measurements for the german cask castor haw 20/28 cg," *Nuclear Thechnology*, vol. 168, no. 3, pp. 867–870, 2017.

[25] C. Wharton, E. Seabury, A. Caffrey, and P. Winston, "Summary report: Inl cdcis cask scanner testing at doel, belgium," Idaho National Laboratory, Tech. Rep., 2013.

[26] C. R. Priest, "Dosimetry, activation, and robotic instrumentation damage modeling of the holtec hi-storm 100 spent nuclear fuel system," Master's thesis, North Carolina State University, MS Thesis 2014.

[27] C. A. Miller and et. al., "Verification of dry storage cask loading using monoenergetic photon sources," *Annals of Nuclear Engineering*, vol. 137, 2020.

[28] R. Kelly and et al., "Uncertainty quantification of concrete utilized in dry cask storage," *Rad. Transport and Pro.*, 2013.

[29] Y. Gao and et. al., "Radiation dose rate distributions of spent fuel casks estimated with mavric based on detailed geometry and continuous-energy," *An. of Nuc. Eng.*, no. 117, pp. 84–97, 2018.

[30] H. Yang, C. Liao, and Z. Liu, "Imaging a dry storage cask with cosmic ray muons," Oregon State University, Tech. Rep., 2018.

[31] C. Liao and H. Yang, "Design of a cosmic-ray muon tomography system for dry storage cask imaging," *IEEE*, 2014.

[32] "Hi-storm fsar," Holtec International, report, 2017.

[33] (2019, Dec). [Online]. Available: https://www.nrc.gov/waste/spent-fuel-storage/dry-cask-storage.html

[34] H. R. Trellue and et. al., "Description of the spent nuclear fuel used in the next generation safegaurds initiative to determine plutonium mass in spent fuel," Los Alamos National Laboratory, report, 2011.

[35] "Scale: Comprehensive modeling and simulation suite for nuclear safety analysis and design," Oak Ridge National Laboratory, report, 2011.

[36] G. I. Bell and S. Galsstone, *Nuclear Reactor Theory*. Von Nostrand Reinhold Company, 1970.

[37] J. J. Duderstadt and L. J. Hamilton, *Nuclear Reactor Analysis*. John Wiley and Sons, 1876.